



Nanoscale

**Characterizing Electronic and Atomic Structures for
Amorphous and Molecular Metal Oxide Catalysts at
Functional Interfaces by Combining Soft X-ray Spectroscopy
and High-Energy X-ray Scattering**

Journal:	<i>Nanoscale</i>
Manuscript ID	NR-MRV-03-2020-002350.R1
Article Type:	Minireview
Date Submitted by the Author:	21-May-2020
Complete List of Authors:	Tiede, David M; Argonne National Laboratory, Chemical Sciences and Engineering Kwon, Gihan; Brookhaven National Laboratory, National Synchrotron Light Source II He, Xiang; Argonne National Laboratory, Chemical Sciences and Engineering Mulfort, Karen; Argonne National Laboratory, Chemical Sciences and Engineering Division Martinson, Alex; Argonne National Laboratory, Materials Science Division

SCHOLARONE™
Manuscripts

Minireview RSC Nanoscale

Characterizing Electronic and Atomic Structures for Amorphous and Molecular Metal Oxide Catalysts at Functional Interfaces by Combining Soft X-ray Spectroscopy and High-Energy X-ray Scattering

David M. Tiede¹, Gihan Kwon², Xiang He¹, Karen L. Mulfort¹, Alex B. F. Martinson³

¹Chemical Sciences and Engineering Division, Argonne National Laboratory, Lemont, Illinois

²National Synchrotron Light Source II, Brookhaven National Laboratory, Upton, New York

³Materials Science Division, Argonne National Laboratory, Lemont, Illinois

Abstract

Amorphous thin film materials and heterogenized molecular catalysts supported on electrode and other functional interfaces are widely investigated as promising catalyst formats for applications in solar and electrochemical fuels catalysis. However the amorphous character of these catalysts and the complexity of the interfacial architectures that merge charge transport properties of electrode and semiconductor supports with discrete sites for multi-step catalysis poses challenges for probing mechanisms that activate and tune sites for catalysis. This minireview discusses advances in soft X-ray spectroscopy and high-energy X-ray scattering that provide opportunities to resolve interfacial electronic and atomic structures, respectively, that are linked to catalysis. This review discusses how these techniques can be partnered with advances in nanostructured interface synthesis for combined soft X-ray spectroscopy and high-energy X-ray scattering analyses of thin film and heterogenized molecular catalysts. These combined approaches enable opportunities for the characterization of both electronic and atomic structures underlying fundamental catalytic function, and that can be applied under conditions relevant to device applications.

Abbreviations

AAO: Anodic Aluminium Oxides; **ALD:** Atomic Layer Deposition; **DFT:** Density Functional Theory; **DRIFTS:** Diffuse Reflectance Infrared Fourier Transform Spectroscopy; **EELS:** Electron Energy Loss Spectroscopy; **EXAFS:** Extended X-ray Absorption Fine Structure; **FTIR:** Fourier-Transform Infrared Spectroscopy; **GCA:** Glass Capillary Arrays; **HAADF-STEM:** High-Angle Annular Dark-Field Scanning Transmission Electron Microscopy; **HEXS:** High-Energy X-ray Scattering; **HR-TEM:** High-Resolution Transmission Electron Microscopy; **IMOC:** Intramolecular Oxygen Coupling; **NEXAFS:** Near Edge X-ray Absorption Fine Structure; **OEC:** Oxygen Evolving Catalysis; **OER:** Oxygen Evolution Reaction; **PDF:** Pair Distribution Function; **PCET:** Proton-Coupled Electron Transfer; **PMMA:** polymethylmethacrylate; **RIXS:** Resonant Inelastic X-ray Scattering; **SEM:** Scanning Electron Microscopy; **SIS:** Sequential Infiltration Synthesis; **TOF:** Turnover Frequency; **UHV:** Ultra-High Vacuum; **XANES:** X-ray Absorption Near Edge Structure; **XAS:** X-ray Absorption Spectroscopy; **XES:** X-ray Emission Spectroscopy; **XPS:** X-ray Photoelectron Spectroscopy.

Introduction

Amorphous thin film materials and heterogenized molecular catalysts supported on electrode and other functional interfaces are of growing, central importance in solar and electrochemical fuels catalysis.¹⁻⁶ A key feature of these interfacial materials is the merging of charge transport properties of conductive and semiconductor supports with discrete sites for charge accumulation and multi-step, bond-making/bond-breaking catalysis. A fundamental understanding of the mechanisms for interfacial electro-catalysis, and ultimately of achieving data-based design of new catalyst materials,⁷⁻⁹ requires resolving atomic and electronic structures of active sites along the sequence of proton-coupled redox steps driving multi-electron bonding-breaking catalysis, and realizing these within a background of the electrode or semiconductor support structures. The complexity of the interfacial catalytic architectures poses a key challenge for resolving structural mechanisms underlying interfacial catalysis. Developments in X-ray light sources and approaches for the analyses of interfacial electronic and atomic structures can be partnered with advances in nanostructured interfacial synthesis to create new opportunities for the resolution of thin film and heterogenized molecular catalysts supported on electrode and other functional interfaces, and applied under conditions relevant to device applications.

For example, transition metal oxides are widely investigated for water-splitting, oxygen-evolving catalysis (OEC) in solar-to-fuels applications.¹⁻⁶ Amorphous transition metal oxides typically show enhanced catalytic performance compared to their crystalline forms.¹⁰⁻¹⁷ Enhanced chemical reactivity can be argued to arise from higher densities of catalytic sites present in the former compared to the latter, presumably associated with the induction of unique coordination structures and defect sites at domain edges.^{14, 18-23} The size of amorphous metal oxide domains ranges from “molecular-dimensioned”, few atom clusters,²⁴⁻²⁷ to the small nanometer scale.²⁸⁻³⁰ A key functional feature of amorphous oxide thin film catalysts is the disordered, linked network of structured domains that is microscopically porous, illustrated in Figure 1. This results in catalytic activities that scale with the 3D film volume rather than the projected 2D surface area.^{31, 32} Catalytic flux is observed to be a product of both the charge transport properties of the networked domains and the intrinsic turnover activities and volume density of the local catalytic atomic sites.^{22, 31-35} Understanding, and ultimately controlling atom site structures and reactivity is a core challenge for catalytic materials design and synthesis.

Similarly, surface-supported, “heterogenized” molecular catalysts are of significant interest because of opportunities to insert catalytic sites based on single or few-atom metal coordination complexes onto conductive supports, and the opportunities to exploit well-developed tools of metal-ligand, and ligand-based outer sphere coordination chemistries to tune chemical reactivity.^{5, 36-43} For example, homogeneous binuclear iridium-oxo coordination complexes designed for water splitting have shown marked enhancements in catalytic turn-over frequency and number (robustness) upon attachment to semiconductor oxide surfaces.⁴⁴ A range of surface spectroscopy and structure probes, including diffuse reflectance infrared Fourier transform spectroscopy (DRIFTS), electron energy loss spectroscopy (EELS) high-angle annular dark-field scanning transmission electron microscopy (HAADF-STEM) demonstrate the preservation of the dinuclear nature of the molecular iridium catalyst when bound to oxide surfaces.^{45, 46} In this case and for heterogenized molecular catalysts more generally, more detailed information on inner and outer coordination shell structures are needed, along with an understanding of how these structures correlation to electronic structure, particularly under solution and operando catalysis. These are critical for understanding ligand and environmental tuning of molecular frontier orbital structures that are

responsible for catalysis. Because of the challenges for achieving detailed structural characterization of heterogeneous interfaces and non-crystalline materials, additional approaches are needed.

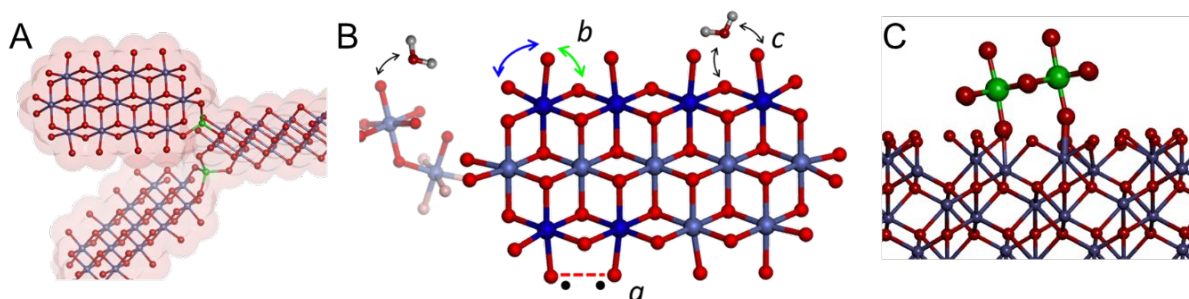


Figure 1. Conceptual structure models for amorphous transition metal oxides and semiconductor surface-bound molecular catalysts illustrating the common feature of catalytic sites at semiconductor surfaces. **Part A.** Illustrates an amorphous oxide modeled as a disordered, 3-D network of persistent structural domains, linked by disordering mono- and di- μ -oxo metal linkages. **Part B.** Domain model for the amorphous cobalt oxide water splitting catalyst film electrolytically formed in the presence of phosphate, $\text{CoO}_x\text{-Pi}$.³⁵ The model includes distortions seen from X-ray PDF data in coordination geometry for terminal oxygen sites.²⁵ Mapped onto this model are schemes for mechanism for the oxygen evolving reaction, OER. These include the accumulation of high valence Co(IV)-oxo or Co(III)-oxyl radicals at domain edge sites (high valence cobalt atoms shaded dark blue). Mechanism for O-O bond formation by intramolecular oxygen coupling or di- μ -oxo bridged water intermediates (red dotted line),²⁰ water nucleophilic attack (black arrows),²¹ geminal oxygen coupling (blue, green arrows),²¹ and possibly slow OER at mononuclear sites.⁴⁹ **Part C.** Model structure for a molecular OER catalyst derived from an iridium (green atoms) di- μ -oxo dimer complex bound to the (001) surface of hematite.⁴⁵ OER mechanisms are proposed to proceed through di- μ -oxo bridged water intermediates.⁴⁵

Advanced characterization techniques such as time-resolved infrared spectroscopies,⁴⁷⁻⁵¹ transition metal K-edge X-ray spectroscopy (XANES, EXAFS),^{21, 24, 52-58} electron microscopy,^{45, 46, 59} surface X-ray diffraction,⁶⁰ and ambient pressure X-ray photoelectron spectroscopy,⁶¹⁻⁶⁴ have achieved milestone advances in the understanding of OER function for both thin-film and surface supported catalysis. Literature cited above and representative recent reviews for interfacial and electrochemical catalysis^{8, 56, 59, 65-69} provide further examples of these advanced techniques.

In this minireview, we focus on emerging opportunities for combined atomic and electronic structure analyses of thin-film oxides and molecular catalysts at electrode and functional interfaces by utilizing opposite ends of the X-ray energy spectrum: soft (< 1 keV) and tender (1-5 keV) X-ray spectroscopy combined with high-energy (> 50 keV) X-ray scattering and atomic pair distance function (PDF) analysis. These are focus areas in X-ray light source and X-ray analysis development.⁷⁰⁻⁷³ Further, the information retrieved from these approaches is complementary. Soft X-ray spectroscopy provides a means to interrogate the details of electronic structures and frontier orbitals that participate catalytic function, while high-energy X-ray scattering provides a direct reciprocal space technique for probing the underlying inner and outer sphere coordination structures with atomic-scale resolution. Advances in the understanding of surface chemistry and catalysis are recognized to be driven by the ability to benchmark quantum theory to experiment.⁷⁴⁻⁷⁶ Particularly for amorphous materials and molecular complexes bound to solid surfaces, active site structures are typically only incompletely defined. Since nuclear structures of materials are correlated to their electronic structures and chemical reactivates through multi-electron interactions, a combination of both soft X-ray spectroscopy and high-energy X-ray scattering analyses

offers opportunities to achieve a more complete interrogation of the electronic and atomic structures that support interfacial catalysis.

A key experimental factor that underlies approaches to combine soft and high energy X-ray analyses is the extreme difference in absorption and scattering cross sections between these X-ray regions. For example, Figure 2 shows a representative layered photocatalytic anode architecture^{77, 78} and the variation of X-ray penetration depth upon going from soft to high energy X-ray regions. The short penetration depth, and corresponding large X-ray absorption cross section, for soft X-rays makes them well-suited, in fact, restricted to probing ultrathin films and interfaces. This places stringent demands on experiments designed to probe operando interfacial catalysis. In contrast, the extremely long penetration depth and corresponding small scattering cross sections for high energy X-rays makes them well-suited to probing inner and outer sphere coordination structures with atomic-scale spatial resolution ($< 0.2 \text{ \AA}$) under operando, device-like conditions, but comparatively poorly suited to probing the thinnest films and planar surfaces.

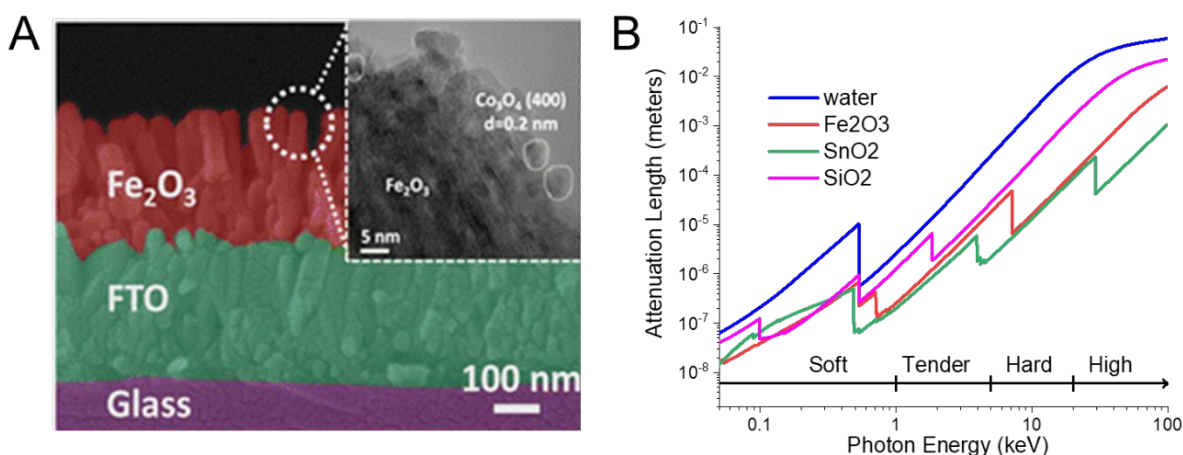


Figure 2. Representative layered photocatalytic anode architecture. **Part A** shows a SEM cross-section of a layered architecture with dimension scale, consisting of a thermally processed hematite layer, conductive fluorine-doped tin oxide layer (FTO) and glass support, rendered in false color. This graphic is reprinted with permission from the Table of Contents graphic from ref. 77. Copyright 2012 American Chemical Society. **Part B** shows energy dependent X-ray attenuation lengths for the materials in each layer of the architecture, reflecting an experimental constraint for soft X-ray analyses. Calculated using NIST X-ray scattering tables.

A connection between these extremes in X-ray analysis is made possible by advances in surface synthesis techniques. These synthesis approaches allow an equivalent electrode-supported catalyst architecture to be designed for experimental access in each X-ray region, and in-turn to be tailored to match device-relevant electrocatalytic chemistry. The use of a shared interfacial catalyst architecture allows combined electronic and atomic structure characterization to be achieved for designed functional interfaces, and suggests new opportunities for interrogating both thin film materials and heterogenized molecular catalysts. This minireview will discuss examples showing how advances in soft X-ray spectroscopy and high-energy X-ray scattering provide complementary approaches for directly interrogating electronic and atomic configurations of amorphous and molecular transition metal catalysts with high resolution, and the interface and materials synthesis that allows these X-ray experiments to be connected.

1. Soft and Tender X-ray Spectroscopy of Interfacial Thin Films and Molecular Catalysis.

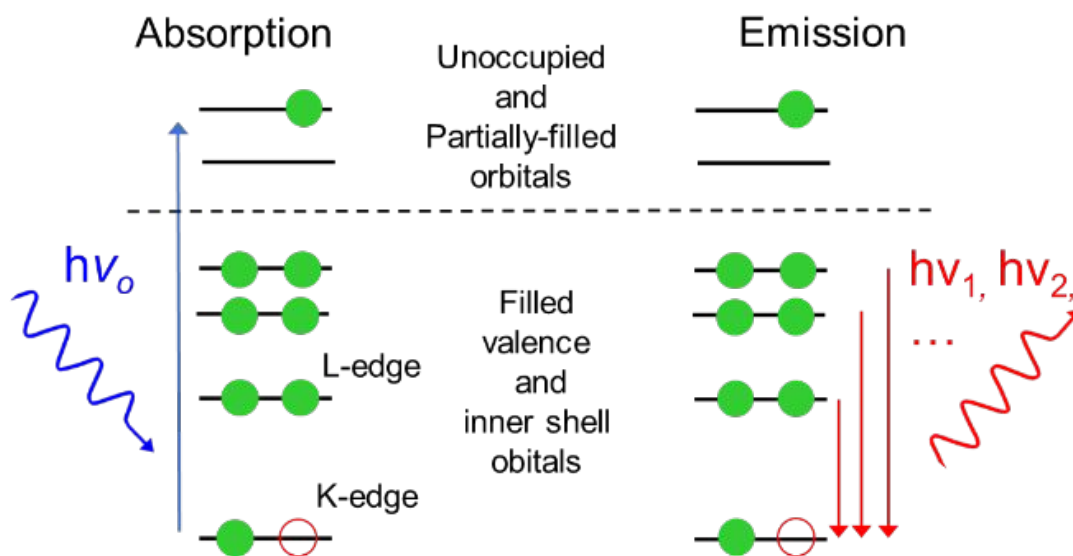


Figure 3. Schematic diagram for core electron X-ray absorption spectroscopy (XAS), resonant X-ray emission spectroscopy (RXES) and resonant inelastic X-ray scattering (RIXS).

Soft X-ray, core electron spectroscopy provides the opportunity to probe electronic structures for thin film and molecular catalysts in an element-specific manner. Co-measurement of electronic structure for both metal and ligand atoms provides a powerful means to interrogate the details of the frontier orbitals that determine catalytic function.⁷⁹⁻⁸³ For C, N, O, S, that are typically involved in coordination to transition metals, or are components of ligand functional groups, K-edge X-ray absorption involves 1s electron excitation to a series of unoccupied or partially filled molecular orbital states, Figure 3. For these elements in organic functional groups, fine structure in the K-edge X-ray absorption spectrum, XAS, shows features reflecting a series of transitions from O 1s to π^* and σ^* hybrid molecular orbital states with energies that are strongly correlated to molecular bonding, hybridization, charge, and environmental effects, such that they can often be used as a spectral "fingerprint" to identify the local bonding environment for the X-ray absorbing atoms.⁸⁴⁻⁸⁶

For oxygen, or other atoms directly coordinated to transition metals, K-edge XAS spectra show a progression of absorption bands involving transitions from the O 1s state to a series of hybrid molecular orbital states with the coordinating metal atom, weighted by the extent of O 2p character in the final state. The first set of absorption peaks involve transitions from O 1s to mixed O 2p-metal 3d states, organized by ligand field splitting, and followed by a spectral region involving transitions from O 1s to O 2p-metal 4s and 4p states.^{57, 84, 87, 88} Ligand atom K-edge transitions are shown to track the extent of covalency in the metal-ligand atom bonding, the ligand field, the number of 3d electrons, and charge states of the coordination complex; all of which are fundamental to the understanding of chemical functionality.^{57, 84, 87, 88}

Electronic structure for metal coordination complex can be tracked in a complementary way from the perspective of the metal atom. For this, metal L-edge XAS for first-row transition metals, (0.1–2 keV) has proven to be particularly effective.⁸⁹⁻⁹² Metal L-edge transitions arise from symmetry-allowed excitation of metal 2p electrons into unoccupied, predominately 3d rich valence molecular orbitals.^{89, 93-95} Transition metal L-edge spectroscopy has been shown to be extremely sensitive to the metal oxidation state, the

ligand field, spin state and the extent of covalency in coordination with ligand atoms, and as such, probe the valence orbitals closely linked to catalytic function.^{89, 93-95} Capabilities for highly resolved X-ray resonant emission spectroscopy, RXES, and related resonant inelastic X-ray scattering, RIXS, spectroscopies are rapidly developing.^{57, 94, 96-99} XAS measures transitions from core to unfilled orbitals and RXES/RIXS provides a complementary measure of transitions between filled orbitals to core holes.^{57, 94, 96, 97} Taken together, XAS with RXES/RIXS provide a means to characterize valence band electronic structures.^{57, 94, 96, 97} RIXS data are typically collected as 2D spectroscopic maps of scanned excitation energy, $h\nu_o$, and measured X-ray emission, $h\nu_n$, from filled orbitals to the core hole, Figure 3. Significantly, for transition metal K-edge RIXS, pre-edge excitation includes $1s$ -to-unoccupied $3d$ absorption and emission from filled $3d$ -to- $1s$ core hole. The difference between excitation and emission energies, and by taking into account multi-electron interactions in the intermediate states, provide a direct measure of d - d ligand field splitting and measurements of the energetics and band structure for the valence orbitals most directly involved in chemical reactivity.^{57, 93, 97, 100-102} These developments in the interrogation of electronic structure by soft XAS and RXES/RIXS have created powerful opportunities to resolve electronic structures underlying catalytic functions for interfacial thin film and molecular catalysts used for OEC.^{57, 94, 96-99} The following examples of soft X-ray spectroscopy analyses applied to OEC provides an introduction to this rapidly expanding field of investigation.

Resolving mechanisms for activation of oxygen ligand atoms in transition metal oxides for OEC. Electronic structures arising from the ligand field of octahedrally coordinated metal-oxo complexes have

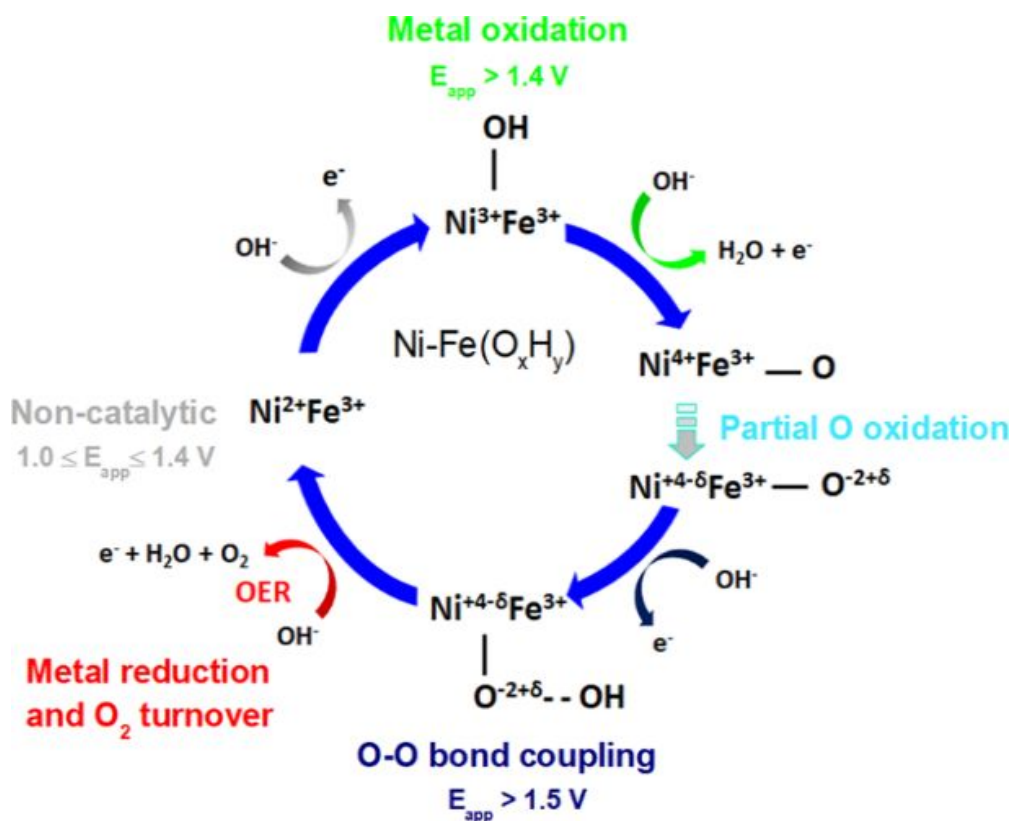


Figure 4. Catalytic scheme identifying a stable intermediate state, $\text{Ni}^{+4-\delta}\text{Fe}^{3+} - \text{O}^{-2+\delta}$, as a precursor to OEC. Reproduced from Drevon et al, 2019, ref 55, with permission under license agreement from Scientific Reports. To view this license, visit <http://creativecommons.org/licenses/by/4.0/>.

suggested general mechanisms for activation of transition metal-oxo complexes for OEC.^{18, 103, 104} Advances in transition metal and O XAS have provided an experimental approach to investigate these fundamental concepts in impressive detail. For example, measurements of metal K-edge and O K-edge XAS have been used to demonstrate the key role that transition metal 3d and the oxygen 2p covalent hybridization plays for activating O atom ligand for OEC in perovskites, ABO_3 (where A is an alkali or rare-earth ion and B is a transition metal).^{103, 105, 106} The extent of covalency in the B-O bond was determined by analysis of the positions and intensities of the O K-edge XAS for a series of perovskites in which the ion A and metal B atoms were systematically varied.¹⁰⁵ OEC activities of the substituted perovskites were shown to track the extent of covalency in B-O bonding, and interpreted to show that increasing O 2p character in the e_g ligand field orbitals promotes OEC by allowing the mixing of electron density and charge through the metal 3d state: $B^{3+}-O^{2-} \leftrightarrow B^{(3+\delta)+}-O^{(2-\delta)-}$.¹⁰⁵ Ligand field tuning of O for OEC was directly interrogated by operando electrochemical metal K- and L-edge XAS and O K-edge XAS measurements for Fe, Ni oxyhydroxides ($Ni-FeO_xH_y$).⁵⁵ In these oxides, O K-edge XAS revealed that partial oxidation of oxygen accompanies the Ni(IV/III) redox transition to form a stable intermediate with an electrophilic oxygen site having oxyl radical character as a precursor to OEC.⁵⁵ This precursor is proposed for function as the site for hydroxyl anion oxidative addition and O-O bond formation as illustrated in the mechanistic scheme, Figure 4.⁵⁵ These results correlate with in-situ *in situ* O K-edge X-ray photoemission and absorption spectroscopy of oxidized O^{2-} and O^{1-} atom species as precursors to OEC in IrO_2 electrocatalysis.¹⁰⁷ These examples show that soft XAS analyses offer an experimental opportunity to directly detect mechanisms for activating ligand oxygen atoms for OEC in mineral oxides.

Soft XAS approaches have been used extensively to investigate other oxides and molecular complexes for OEC.⁵⁷ For example, cobalt K- and L-edge XAS and cobalt K-edge RIXS were used to analyze the electronic structure of a cobalt-oxo cubane, $Co_4O_4(\text{acetate})_4(\text{pyridine})_4$, in the Co(III)₄ and the first one-electron oxidation state of the complex.¹⁰⁸ The XAS/RIXS methods were shown to probe the extent of “localized” Co(IV) electronic structure among the cubane core and permitted an analysis of the extent of electronic hybridization between Co 3d and O 2p states, thus providing an approach to investigate the evolution of electronic structures in catalytic cobalt cubane cores.¹⁰⁸

Resolving electronic structures underlying charge transport in thin-film oxides. A characteristic aspect of thin-film transition metal oxide OEC function is the convolution of catalytic activity at the active sites with the charge transport properties of the oxide films.^{22, 31-35} This is reflected in the significant variation of OEC activity that arises by varying the metal content and anions used as the electrolyte during electrochemical film deposition.¹⁰⁹⁻¹¹⁴ Electrochemical analyses show that the catalytic activities are determined by a combination of parameters, including the number density of catalytic sites, intrinsic catalytic rate, electrochemical over-potential, proton and charge transport properties of the films.^{19, 21, 22, 28, 31-34}

For example, catalytic activities for amorphous cobalt (oxy)hydroxides thin films formed by anodic electrochemical deposition vary characteristically depending upon the anions used in the electrolyte solutions.^{110, 113, 115, 116} The process for electrochemical deposition from aqueous cobalt solutions containing phosphate (Pi), methyl phosphate (MePi), and borate (Bi) as anions in the electrolyte have been studied in particular detail,^{110, 115, 116} and the oxyanions are understood to limit layering and cobalt (oxy)hydroxide domain growth to different extents.^{25, 28, 29} Correlations between the bulk catalytic and conductive properties for the OEC with electronic structures for the cobaltate domains have been probed by Co L-edge XAS and K-edge XES/RIXS.³⁵

In particular, Co L-edge XAS and K-edge RIXS have been used to compare electronic structures of the amorphous cobalt (oxy)hydroxide formed in the presence of phosphate, $\text{CoO}_x\text{-Pi}$, versus borate, $\text{CoO}_x\text{-Bi}$, during electrochemical deposition.³⁵ Both catalysts share a common cobaltate core structure,^{25, 28, 29} but differ significantly in OER performance. For example, Figure 5A shows a plot of turnover frequency, TOF, per cobalt atom measured at variable fixed over-potentials as a function of the thicknesses of the amorphous $\text{CoO}_x\text{-Pi}$ and $\text{CoO}_x\text{-Bi}$ catalyst films.³⁵ Sites for OEC within $\text{CoO}_x\text{-Pi}$ and $\text{CoO}_x\text{-Bi}$ catalyst films have been shown to be uniformly distributed throughout the full 3D film volume, rather than being restricted to the 2D surface area.³² The attenuation with TOF with increasing film thickness is understood to arise from charge transport impedance within the films.³¹⁻³³ The 1.6-fold difference in slopes for the plots in Figure 5A shows that the $\text{CoO}_x\text{-Bi}$ has a lower film-thickness dependent impedance compared to $\text{CoO}_x\text{-Pi}$, although the crossing of the curves with diminishing film thicknesses indicates that the catalytic rate for $\text{CoO}_x\text{-Pi}$ on a per atom basis is higher than that for $\text{CoO}_x\text{-Bi}$.^{28, 35} This has been interpreted to be a consequence of the smaller domain size for $\text{CoO}_x\text{-Pi}$ compared to $\text{CoO}_x\text{-Bi}$, discussed further in Section 2 below, with the phosphate form of the catalyst having a higher density of active domain edge sites.^{28, 35} In terms of differing electronic properties, conductance measurements of films in the absence of electrolyte show the conductivity of $\text{CoO}_x\text{-Bi}$ to be 60-fold higher than that of $\text{CoO}_x\text{-Pi}$.³⁵ Hence, both electrocatalytic current measurements and the intrinsic conductance properties of the catalysts as bulk films show that the Bi form of the amorphous oxide supports higher charge transport than the Pi form.^{28, 35}

35

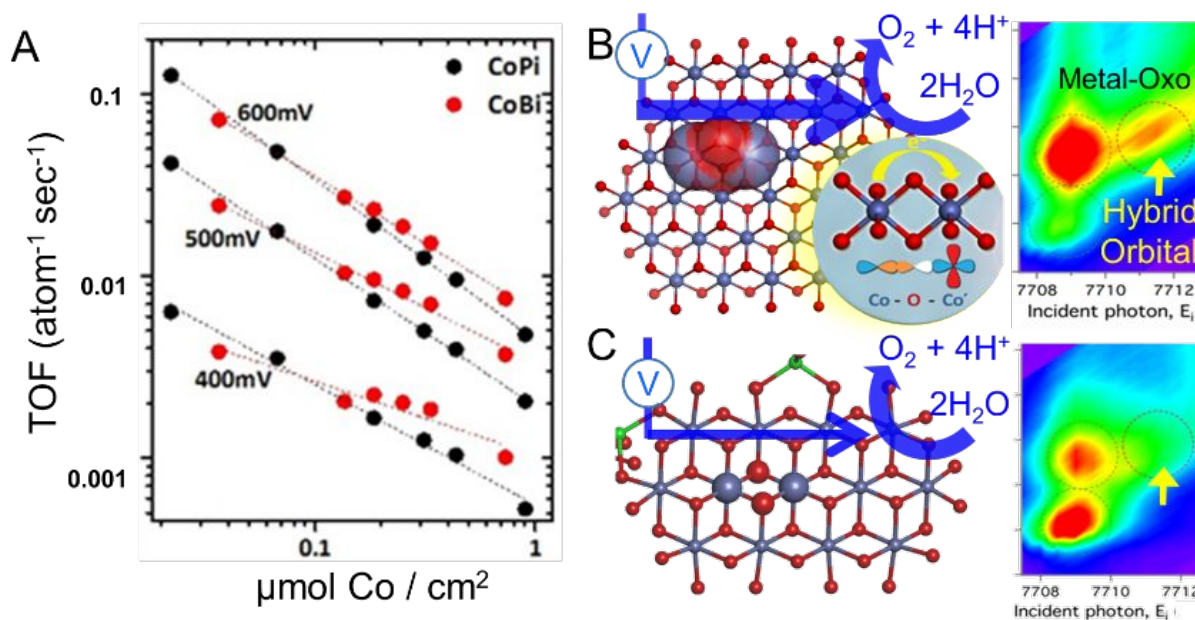


Figure 5. Resolution of atomic and electronic structures underlying catalytic function for $\text{CoO}_x\text{-Pi}$ and $\text{CoO}_x\text{-Bi}$ forms of amorphous cobalt (oxy)hydroxide OEC thin films. Part A shows the per cobalt atom turnover frequency, TOF, measured for $\text{CoO}_x\text{-Pi}$ and $\text{CoO}_x\text{-Bi}$ at different overpotentials (vs NHE) as a function of film thickness, measured by the number of cobalt atoms/ cm^2 . Parts B and C show domain models for $\text{CoO}_x\text{-Bi}$ and $\text{CoO}_x\text{-Pi}$, respectively, determined by high energy X-ray scattering (HEXS).^{25,28,29} Superimposed are indications of the differing extents of inter-site delocalized orbitals, determined by Co K-edge RIXS, right panels.³⁵ Figure adapted with permission from ref 35. Copyright 2018 American Chemical Society.

Co L-edge XAS and K-edge RIXS have shown that differences between catalytic and dry conductance properties of the borate and phosphate forms of the amorphous cobalt oxyhydroxide catalysts can be traced back to differences in electronic structure measured at the atomic scale. Co L-edge XAS showed that $\text{CoO}_x\text{-Pi}$ and $\text{CoO}_x\text{-Bi}$ differ in the presence of a significant fraction (17%) of tetrahedral Co(II) defect atoms in $\text{CoO}_x\text{-Pi}$ compared to the absence in $\text{CoO}_x\text{-Bi}$.³⁵ Further, Co K-edge $1s3p$ and $1s3d$ RXES/RIXS showed that the two forms of CoO_x differ significantly in oxygen-mediated, inter-site metal coupling, delocalized orbitals that are present in $\text{CoO}_x\text{-Bi}$ but absent in the Pi form.³⁵ The difference in inter-site electronic coupling was found to correlate with the enhanced conductivity and band transport properties of $\text{CoO}_x\text{-Bi}$ compared to $\text{CoO}_x\text{-Pi}$ in the dry state³⁵ and the redox-linked charge transport properties during wet electrocatalysis.^{28, 31-33, 35} The cause for disruption of inter-site coupling in $\text{CoO}_x\text{-Pi}$ compared to the Bi form is of interest since this seems to limit electrocatalysis in a material that otherwise might be positioned for enhanced OEC because of the higher number density and intrinsic TOF of the catalytic sites. Co K-edge RIXS showed significant line broadening for the $1s3d$ transitions in $\text{CoO}_x\text{-Pi}$ compared to those in $\text{CoO}_x\text{-Bi}$ and the reference LiCoOOH material.³⁵ This together with optical resonance Raman³⁵ and PDF data,²⁵ suggests that a significant “ligand field strain” or coordination geometry disorder exists among the cobalt atoms within the $\text{CoO}_x\text{-Pi}$ domains. This suggests the possibility that the greater extent of coordination geometry or ligand field disorder in $\text{CoO}_x\text{-Pi}$ compared to $\text{CoO}_x\text{-Bi}$ may be correlated to a less efficient mixing of orbitals between atomic sites and result in the differences observed in charge transport efficiencies between these two catalytic materials.

Complementary analyses of O K-edge XAS on $\text{CoO}_x\text{-Pi}$ have also shown the presence of a pre-edge peak characteristic of empty oxygen p orbital hybridization with cobalt $3d$ orbitals, and that the presence of this band scales with Co(III) oxidation state content.¹¹⁷ Delocalized, oxygen-mediated inter-site coupling transition have been further analyzed in mineral forms of the cobalt oxides,^{100, 118, 119} and more generally among electronically active metal oxide materials.^{57, 93, 97, 101, 102, 108, 120} In-situ, electrochemical Co K-edge $1s3p$ RIXS measurements show that the inter-site transition for CoOOH attenuates with the accumulation of Co(IV) valence sites and at electrochemical potentials sufficiently high to enable OEC.¹¹⁸ These and the preceding discussion illustrates opportunities to utilize advances in soft X-ray spectroscopy to investigate the progression of electronic structures that accompany multi-step fuels catalysis.

Advances in surface synthesis enabling operando soft X-ray interrogation of interfacial catalysis.

Advances in nanoscale interface design and synthesis open additional opportunities for soft X-ray interrogation of interfacial catalysis under device and applications relevant conditions. For example, X-ray window, electrode “chip” assemblies have been designed to handle the short, 100 nm scale penetration depths for soft X-rays and the need to work in high vacuum beamline environments to enable soft XAS operando electrochemical measurements.¹²¹⁻¹²⁴ A schematic diagram of a recently implemented X-ray electrode chip is shown in Figure 6A,¹²⁵ configured to function as a high vacuum X-ray window and as a working electrode for an electrochemical cell, Figure 6B, and which could be configured for total fluorescence yield or X-ray emission detection.¹²¹⁻¹²⁴ An alternate design for a liquid electrochemical cell for soft XAS is shown in Figure 6C.^{55, 126} A key feature of these operando cells is the multilayer electrode architectures. These exploit capabilities in lithography and interfacial synthesis to create multilayer architectures that are fabricated to provide short, 100 nm scale soft X-ray path length to access the catalytic films while maintaining functional electrochemical connections and compatibility with an ultra-high vacuum (UHV) X-ray environment. Further innovations for accomplishing soft X-ray measurements

of catalysts under operando conditions include experimental designs for UHV exposed surface solvent layers⁶⁴ and submicron liquid jets.¹²⁷

The 100 nm scale penetration depth for soft X-rays makes them well-suited for interrogating the bulk electronic properties of catalyst films of comparable dimension. However, this limits the sensitivity of soft XAS for the few atom layers at surfaces, and particularly for electrode and surface-supported, heterogenized molecular catalysts that are of wide-spread interest for solar and electrochemical fuels applications.^{5, 36-43} The examples discussed above have been applied for the characterization of bulk thin film catalysts. However, opportunities exist to extend soft XAS analyses to sharp interfaces and surface-supported molecular catalysts by exploiting the synthesis of nanostructured, high surface area supports to realize porous scaffolds with thicknesses matched to the attenuation depth of soft X-rays. Examples include N 1s XAS fine structure analyses of metallated and free base protoporphyrin dyes bound to nanostructured ZnO Surfaces¹²⁸ and Fe and Ni K- and L-edge XAS OEC clusters on nanostructure carbon “paper” electrode supports.¹²⁹ These approaches build on advances in scaffold and surface synthesis. Further opportunities for development lie in the need to extend these synthetic approaches to make concomitant analyses of electronic and atomic structure, for example by enabling interfacial catalyst characterization using high-energy X-ray scattering and PDF analyses discussed in the following section.

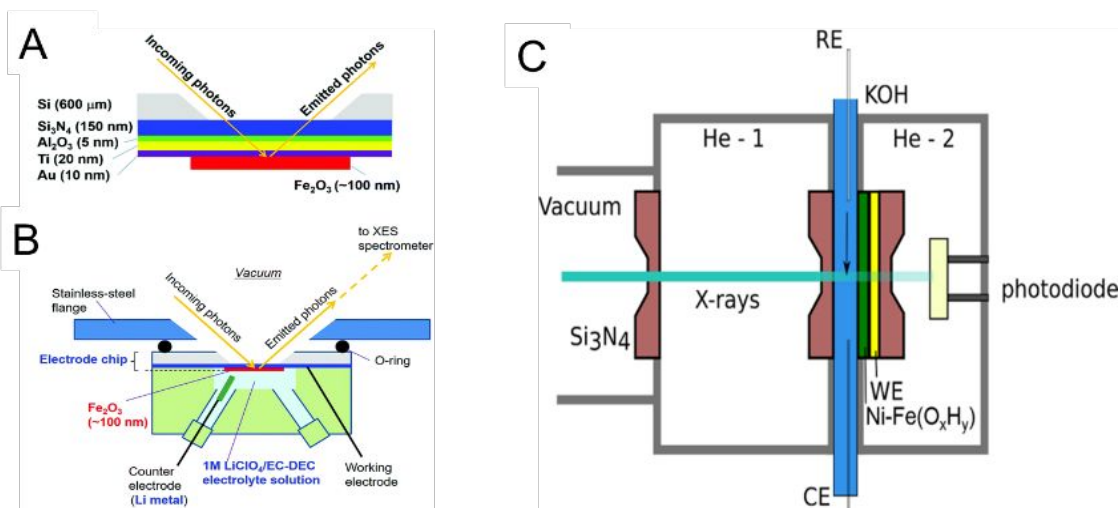


Figure 6. X-ray window, electrode “chip” assemblies for electrochemical soft XAS. Schematic pictures for (a) the electrode chip and (b) operando XES cell. Reproduced from Ref. 125, with permission from the PCCP Owner Societies. Part C shows a design scheme for a liquid electrochemical cell for soft XAS, reproduced from ref. 55 under license agreement from Scientific Reports. To view a copy of this license, visit <http://creativecommons.org/licenses/by/4.0/>

2. High-Energy X-ray Scattering for Atomic Structure Interrogation of Thin Film and Interfacial Molecular Catalysts.

A key feature of catalysis is the site-specific tuning of structures that leads to the activation of bond-making and bond-breaking chemical reactivity. The advances in soft and tender X-ray absorption and related hard X-ray emission spectroscopies described above are exciting because of the opportunities these have created for resolving electronic configurations of transition metal catalysts at functional interfaces and operando conditions, and to identify how transition metal electronic configurations are linked to chemical reactivity. A further challenge lies in resolving the atomic structures that underpin the

tuning of catalyst electronic configurations. Resolution of the interplay between atomic and electronic structures, described by multi-electron theory, is necessary for the development strategies to achieve advanced catalyst designs. Extended X-ray absorption fine structure (EXAFS) is a familiar and widely-applied approach for interrogating transition metal coordination structures for transition metal catalysis at functional interfaces and under operando conditions.^{21, 24, 52-58} In the following, we discuss an emerging opportunity for coordination shell structure resolution relevant to interfacial catalysis through high angle X-ray scattering and atomic pair distribution function (PDF) analysis.¹³⁰⁻¹³⁹ Compared to EXAFS analysis, HEXS-PDF offers opportunities for structure characterization across a broader range of inner and outer coordination shell distances than can be typically accessed by EXAFS analysis alone. Emerging work is demonstrating opportunities to extend HEXS-PDF analyses for the characterization of transition metal catalysis at functional interfaces and under operando conditions. Significantly, the interfacial synthesis approaches being developed for interfacial HEXS-PDF analysis are analogous to those used for operando soft XAS, and hence these introduce opportunities for combined atomic structure and electronic configuration analysis using reciprocal space X-ray techniques, EXAFS and HEXS-PDF, combined with soft X-ray and atomic spectroscopy analyses.

HEXS-PDF provides opportunities to probe molecular and materials structures with a spatial resolution that can be extended to 0.1 Å.¹³⁰⁻¹³² The high spatial resolution and penetration depth for high energy X-rays make PDF well-suited for in-situ and operando characterization of catalysts.¹³³⁻¹³⁹ Atom pair distances measured by PDF are useful complements to those determined by EXAFS analyses. The two approaches provide atom pair distances measured with comparable spatial resolution, however, EXAFS provides an element-selective measurement of X-ray absorbing atom-to-neighboring atom pair distances,^{140, 141} while PDF provides an all-atom measure of pair distances.¹³⁰⁻¹³² For amorphous and disordered molecular materials, we have found that atom pair distances resolved by EXAFS are often limited to primarily the first, and possibly second coordination shells. In contrast, PDF can resolve a more complete set of atom pair distances across a wider range of inner and outer shell coordination distances.

To illustrate the different extents of outer sphere structure resolution, Figure 7 compares EXAFS and PDF data collected for three different metal oxide oxygen-evolving catalysts. Figures 7A and B show EXAFS and PDF data for amorphous CoO_x-Pi^{24, 25} and amorphous IrO_x^{26, 142} catalyst film materials, respectively. Figure 7C shows EXAFS and PDF data measured for an iridium-oxo dimer homogeneous OEC molecular complex in aqueous solution.¹⁴³ In each case, EXAFS and PDF are seen to provide an accurate measure of the 1st shell metal atom-to-ligand atom pair distances. However, 2nd sphere oxo-bridged, metal-to-metal pair peaks are measured with variable, lower intensity. Note that the EXAFS plots are not corrected for scattering path dependent phase corrections.^{140, 141} This causes the apparent shifts in peak positions between the plotted EXAFS and PDF data. For all three catalysts, the PDF measurements are seen to resolve the 1st metal atom coordinate distance and a set of longer-range pair distances that are not resolved or only poorly resolved by EXAFS measurements. The three sets of PDF data were found to be sufficient for quantitative structure model testing. Best-fit structures for the amorphous metal oxide domains and molecular coordination complex are shown in the insets.^{25, 26, 143} The structure selected by fitting to PDF data alone does not necessarily yield a unique structure solution, but a representative structure whose distribution of atom pair distances match those in experiment. The iridium-oxo dimer molecular complex shown in Figure 7C was determined using a combination of solution EXAFS and PDF data to screen and select a best-fit structure from a library of candidate structures derived from DFT calculations.¹⁴³ A structure for this complex was subsequently determined crystallographically^{144, 145} and

demonstrated the validity of using a combination of in-situ EXAFS and PDF measurements with DFT structure modeling as an approach to achieve de novo structure determination.¹⁴³ This study

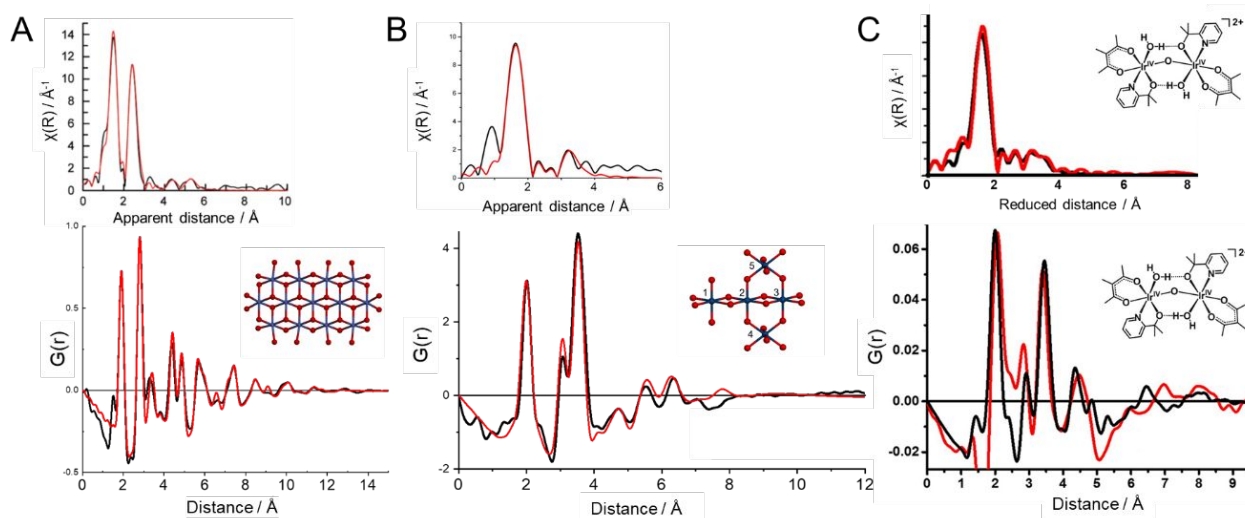


Figure 7. Comparison of EXAFS and PDF for amorphous oxides and a molecular OEC coordination complex. **Part A** shows a comparison for the amorphous $\text{CoO}_x\text{-Pi}$ catalyst. The EXAFS data are reprinted with permission from ref. 24. Copyright 2010 American Chemical Society. The structural model inset and PDF were as described in ref. 25. **Part B** shows data for the amorphous iridium oxide “blue layer” thin film catalyst. EXAFS are reprinted with permission from ref. 142. Copyright 2013 American Chemical Society. PDF data and amorphous domain structure model were described in ref. 26. **Part C** show data for an iridium-oxo dimer molecular catalyst. The data are reprinted with permission from ref. 143. Copyright 2016 American Chemical Society. For each panel atom pair distance distributions measured by EXAFS are on top and those measured by HEXS and PDF analysis are on the bottom. In each case, the black line traces show experimental data, red line traces show calculated patterns based on coordinate models. For each of the PDF panels, and for the EXAFS data in Part C, the coordinate models shown in the insets were determined by fitting to the experimental data. For Parts A and B, EXAFS data were fit to simpler minimal models.

demonstrates the validity of HEXS PDF analysis for atomic structure interrogation when single crystal structure determination is impractical or impossible as is the case for many amorphous and heterogenized materials and molecules.

The ability of PDF to determine outer sphere atom pair distances with sub-angstrom resolution provides opportunities to resolve local site structures that cannot be achieved by other methods. This is illustrated by the PDF analysis of domain structure in amorphous $\text{CoO}_x\text{-Pi}$.^{25, 28, 29} Figure 8A shows a comparison of experimental and calculated PDF using a 13 cobalt atom cobaltate structure, model **1**. The model provides good agreement with the experimental PDF, although discrepancies are seen for the pair correlation peaks labeled *c*, *g*, corresponding to Co-O distances that include contributions from both lattice and terminal oxygen atom sites indicated in the inset. Figure 8B shows the improvement in PDF fitting upon introducing slight displacements to the coordination geometries for the terminal oxygen atoms, resulting in approximately 0.25 Å shifts in position.²⁵ The scale of these displacement demonstrates the sensitivity of PDF for detecting fine structure changes that may be critical to function. These results further provide a demonstration of the ability to use PDF to detect differences in coordination geometries between edge and lattice site locations in the cobaltate domains, and therefore, an opportunity to track site-dependent chemical reactivity. These aspects are discussed further with extension to operando electrochemical PDF

analysis discussed below. While PDF analysis has been shown to provide a powerful tool for the characterization of solution, bulk, or thick film amorphous and non-crystalline molecular materials,¹³³⁻¹³⁹ a key challenge lies in the development of techniques for the in-situ and operando PDF characterization of ultrathin catalytic films and interface-supported molecular catalysts.

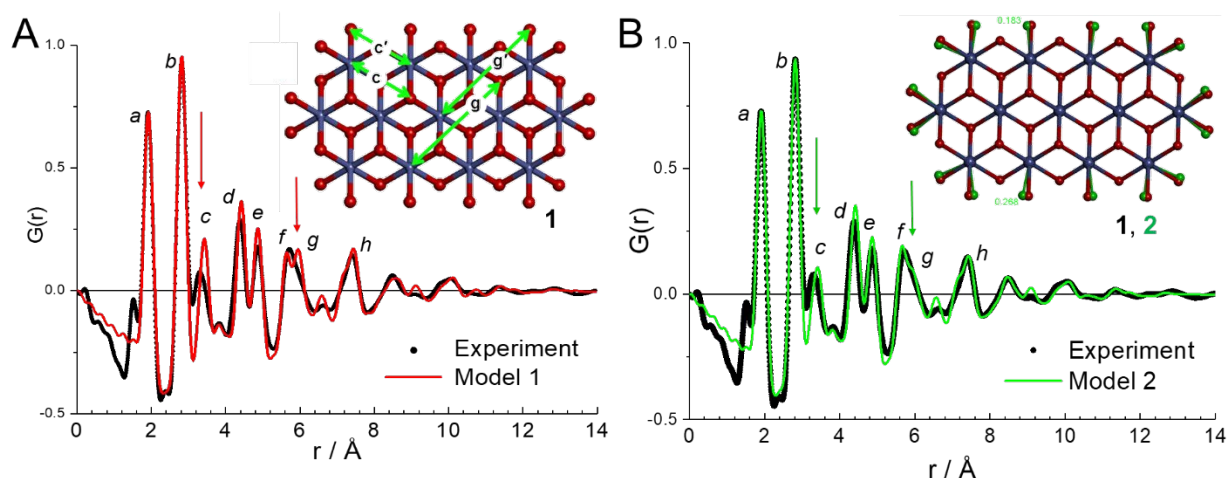


Figure 8. PDF Resolution of distortions in coordination geometry in the amorphous CoO_x -Pi domain structure. **Part A** shows experimental (black) and calculated (red) PDF for a cobaltate domain model structure **1** (inset). The arrows mark specific pair correlation, c, g which show mis-matched between the experiment and model. These atom pair distances are marked on the in-set and involve Co-O atom pairs in the lattice and terminal oxo edge sites. **Part B** shows experimental (black) and modified model **2** (green) PDF for a cobaltate domain model structure, shown super-imposed on the model **1** structure. Compared to **1**, model **2** contained random coordination geometry distortions corresponding to position displacements of about 0.25 \AA . The calculated PDF shows an improved fit to data. The experimental also so a pair peak at 1.5 \AA corresponding to the P-O pair distance for phosphate which is absent from these models. See ref. 25 for further information.

PDF analysis of ultrathin films and interfacial molecular catalysts. The small scattering cross section (deep penetration depth) for HEXS places significant constraints on detection and PDF analyses from ultrathin films and interfacial catalysts, particularly under operando electrochemical conditions. We have investigated strategies for investigating structures of ultrathin films and interfacial catalysts. Here we illustrate opportunities for thin film and few-atom metal cluster characterization by presenting examples of PDF characterization of metal oxides fabricated by sequential infiltration synthesis, SIS.¹⁴⁶ SIS is an emerging technique for the synthesis of organic polymer-templated transition metal oxides.^{147, 148} SIS builds upon sequential, saturating, gas phase reactions of atomic layer deposition, ALD, but utilizes functional handles within polymers. Selective SIS can be achieved in thin films with nanoscale organization as routinely produced through phase-segregating block co-polymer.^{149, 150} Inorganic replicates of the polymer nanopatterns are achieved through metal-atom coordinating functional groups within selected polymer blocks which act as nucleation sites for metal-oxo complex assembly. Successive cycles of SIS-ALD synthesis provide a mechanism to achieve a controlled, element-by-element assembly of metal-oxo clusters through precisely choreographed precursor introduction and purging. Etching techniques and thermal processing can be used to anneal the SIS metal oxides and remove the organic components, leaving only inorganic oxides.^{149, 151} We have interrogated indium oxide SIS ALD assembly processes in polymethylmethacrylate, PMMA, spin-coated thin films by tracking SIS $\text{In}(\text{O})_x(\text{OH})_y$ cluster growth using a combination of SEM/TEM, FTIR,¹⁵¹ In K-edge EXAFS, and HEXS-PDF analyses.¹⁴⁶ The nucleating and few-

atom clusters formed during the sequence of individual SIS ALD cycles serve as benchmarks for assessing capabilities for high-resolution PDF characterization of interfacial few-atom clusters and molecular catalysts, and demonstrate the merit of a PDF approach to investigate mechanisms underlying SIS.

Figure 9 shows a plot of SEM thicknesses and atom percentage of $\text{InO}_x(\text{OH})_y$ in hybrid films formed by SIS infiltration into spin-coated PMMA films, and plotted as a function of the number of SIS cycles.¹⁵¹ The

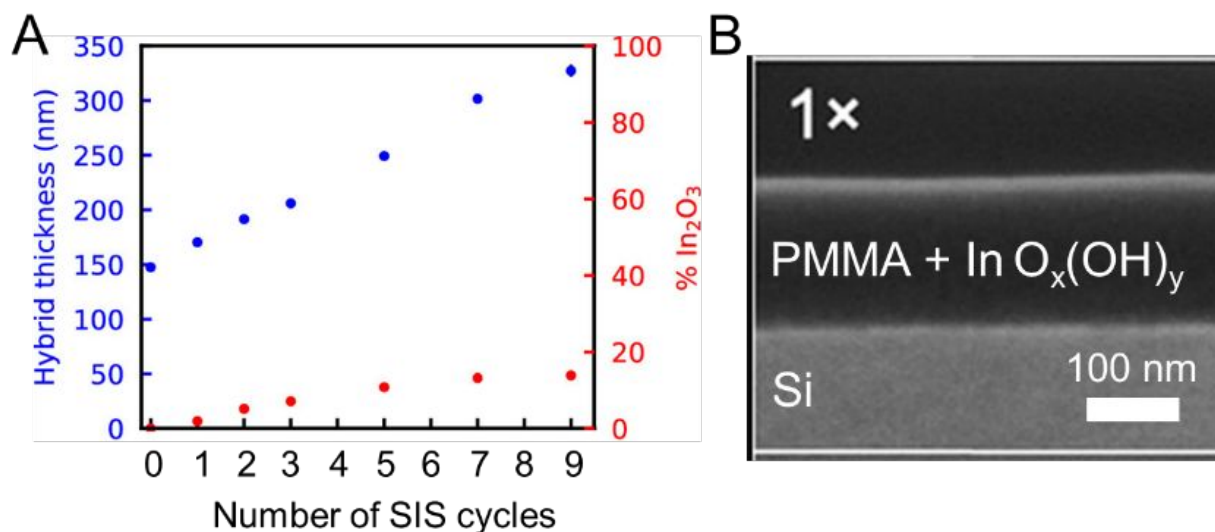


Figure 9. Cross sections of hybrid SIS $\text{InO}_x(\text{OH})_y$ /PMMA films. **Part A.** Shows SEM measured thicknesses (left axis) and atom percentages of $\text{InO}_x(\text{OH})_y$ (right axis) for the hybrid films as a function of number of sequential ALD synthesis cycles. **Part B.** Shows an example of a SEM cross-section for the 1x SIS hybrid film. Reprinted with permission from ref. 148. Copyright 2013 American Chemical Society.

hybrid film thickness is seen to progressively swell from an initial PMMA film thickness of about 100 nm to approximately 340 nm following 9 SIS cycles.¹⁵¹ We found that PDF characterization is able to provide critical new information on the nucleation and few-atom clusters formed during the initial stages of SIS.¹⁴⁶ Figure 10A shows PDF patterns measured for hybrid SIS $\text{InO}_x(\text{OH})_y$ /PMMA films as a function of the number of SIS cycles.¹⁴⁶ PDF of the $\text{InO}_x(\text{OH})_y$ clusters formed during the first ALD cycle show characteristic atomic pair distances that correspond to mono- and di- μ -oxo-linked indium dimers, but no pair correlations at longer distances. The analysis suggests that the SIS nucleating clusters can be described by a combination of the dinuclear clusters **1** and **2** and the trinuclear cluster **3**, shown in Figure 10B.¹⁴⁶ The finding of predominately di- and tri-nuclear clusters is remarkable since it suggests that the mechanisms and atomic mobility in the initial nucleating phase of SIS in PMMA differ from those in traditional surface ALD synthesis on oxide supports.¹⁴⁶ Tracking of the $\text{InO}_x(\text{OH})_y$ clusters in subsequent SIS cycles reveals that the $\text{InO}_x(\text{OH})_y$ clusters can be understood to react and further grow by indium addition to the terminal oxo sites on the nucleating clusters **1-3**, causing a predominately linear growth format for the clusters.¹⁴⁶ High-temperature annealing uniformly converts the SIS $\text{InO}_x(\text{OH})_y$ clusters that result from all number of SIS cycles to a similar nanocrystalline cubic In_2O_3 final structure. The detection of nucleating di- and tri-nuclear 1x SIS cycle $\text{InO}_x(\text{OH})_y$ clusters, and the deciphering of the mechanism for SIS cluster growth demonstrate clear opportunities to implement high-resolution, in-situ PDF analyses for characterization of few-atom cluster and molecular catalysts.

The PDF of the $\text{InO}_x(\text{OH})_y$ in hybrid films shown in Figure 10 were obtained using two different scattering geometries.¹⁴⁶ The first used a transmission scattering geometry, illustrated in Figure 10C, on PMMA films spin-coated onto 100 nm thick silicon nitride windows, and interrogated using 58.7 keV X-ray scattering. The thin silicon nitride support was necessary for minimizing background scattering and to enable detection of scattering from the thin, SIS hybrid films. In this configuration, the PDF analysis with high signal-to-noise with a spatial resolution of 0.2 Å required 50 minutes of data acquisition for each of the sample and background images at beamline 11-ID-B of the Advanced Photon Source. A second experimental geometry used the recently introduced technique of grazing incident PDF, GI-PDF, with 86.7 keV X-rays, figure 10D.¹⁵² GI-PDF proved to be a much more efficient data acquisition technique, allowing comparable signal-to-noise and spatial resolution to be achieved with 50-fold shorter data acquisition times compared to the transmission scattering geometry. GI-PDF offers a significant advance by enabling a more rapid collection of HEXS for PDF characterization of ultrathin films and interfacial chemistry.¹⁵² The increased sensitivity for the GI-PDF measurement compared to the transmission geometry arises in part from the increase in the area of incident X-ray footprint, with corresponding increase in the volume of the film that is interrogated by X-rays, compared to the transmission geometry. Follow-on development for operando and functional-catalysis PDF will need to consider approaches for the incorporation of electrochemical interfaces and time-resolved techniques.

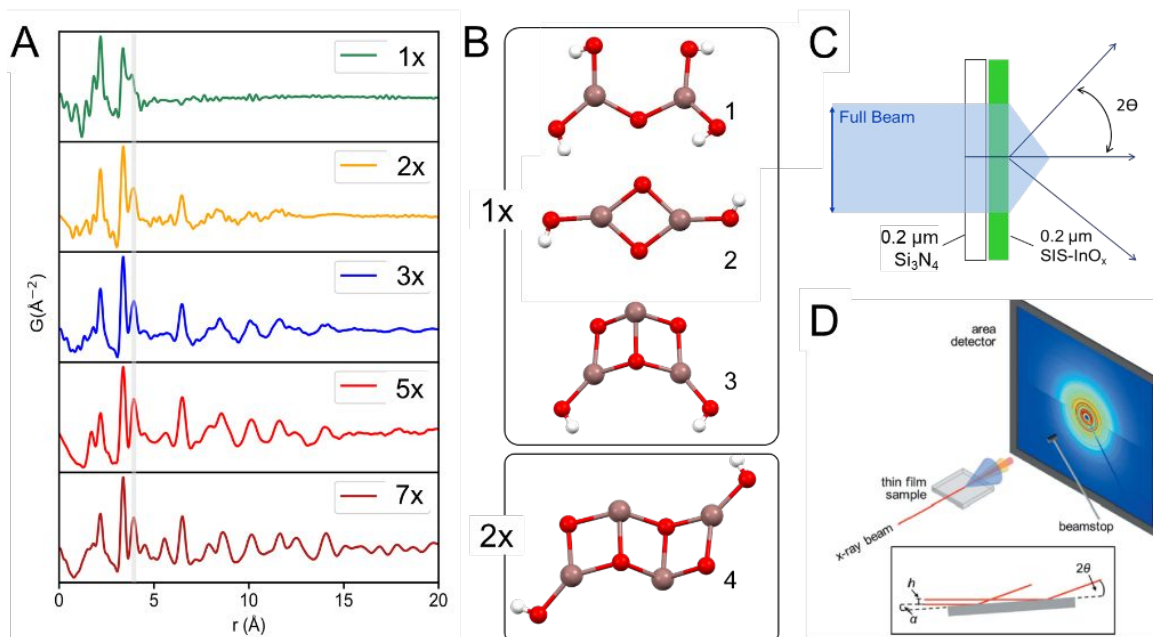


Figure 10. PDF analysis of hybrid SIS $\text{InO}_x(\text{OH})_y/\text{PMMA}$ films. **Part A** shows PDF patterns measured for the hybrid films following 1, 2, 3, 5, 7 SIS-ALD cycles, indicated by the inset labels. **Part B** shows $\text{InO}_x(\text{OH})_y$ cluster models that can be used to fit the data. The 1x, 2x, 3x PDF were measured using the transmission geometry, **Part C**, and the 5x and 7x PDF were measured using a grazing incidence geometry, **Part D**. The PDF data and structures are described in ref. 146. The grazing incidence experiment geometry, **Part D**, is reproduced from ref. 152 with permission from the IUCr.

Extending PDF to electrochemical operando characterization of interfacial catalysis. PDF techniques have been developed to investigate structures and electrochemical mechanisms of micron-scale electrodes and redox-active materials, particularly with respect to battery and energy storage processes.¹⁵³⁻¹⁵⁷ A high surface area capillary working electrode designed for PDF analysis of nanoparticles, and possibly additionally suitable for PDF analysis of homogeneous molecular metal complex catalysts, has also been described.¹⁵⁸ We have introduced high-surface area, micro- to nano porous working electrodes and electrochemical cells as an approach to achieve high-resolution PDF for thin interfacial catalyst films during electrochemical operation.¹⁵⁹ In this approach glass capillary arrays, GCA, or anodic aluminum oxides, AAO, were chosen as porous scaffolds with pore diameters that range from 100 microns to 20 nm, and provide 10 to 10^4 increases, respectively, in HEXS signal intensity compared to a planar 2D interface.¹⁵⁹ A key feature of this approach is the ability to use ALD to create conductive and tailored interfaces conformally coated on the 3D porous substrates. This approach creates a high surface area replicate of device and “electrode chip” interfaces used in soft X-ray spectroscopy to enable electronic structure analysis by soft X-ray spectroscopy and atomic structure analysis by PDF of the same microscopic system. For example, Figure 11A shows real-time monitoring of the growth of an amorphous CoO_x -Pi OEC film measured at continuous intervals during electrochemical deposition by HEXS peak scattering.¹⁵⁹ HEXS intensities could be calibrated to film thickness measured by SEM, Figure 11B, and show that with 40 μm pore diameter GCA substrates, PDF analysis is possible for amorphous first row transition metal oxides with a film thickness of only 60 nm.¹⁵⁹ The HEXS signal scales with the 3D working electrode surface area, and on-going work shows that by selecting AAO supports with comparable porosity, but with pore dimensions on the 10 nm scale, PDF analyses can readily be extended to investigate sub-nm films as well as supported molecular catalysts assemblies with effective thickness of ~ 1 nm.

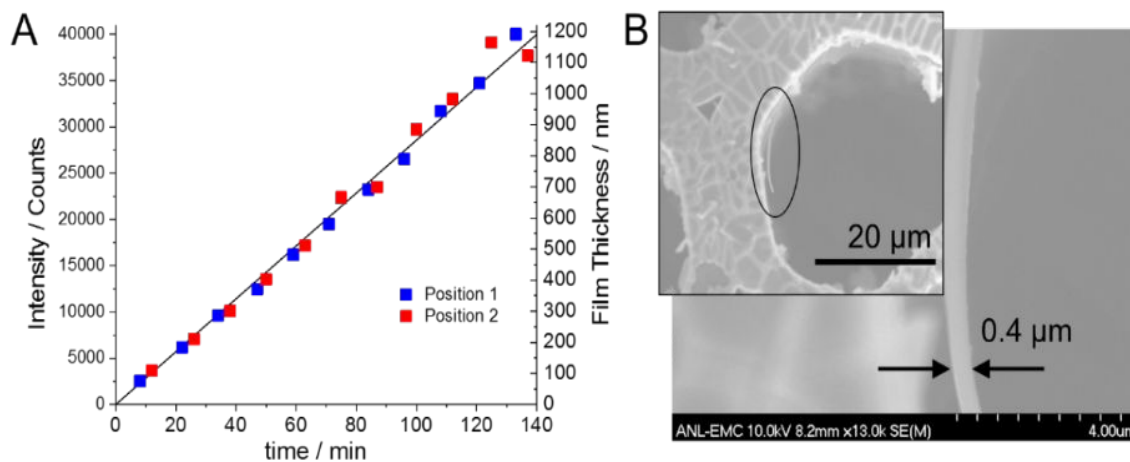


Figure 8. In-situ tracking CoO_x -Pi electrochemical film deposition. **Part A.** Plot of HEXS signal intensity at selected times during the continuous electrochemical deposition. The scattering intensity was measured by the amplitude of the peak feature at $q = 4.5 \text{ \AA}^{-1}$, and recorded for two positions along the ITO/GCA pore. **Part B.** SEM image of CoO_x -Pi film on the ITO/GCA electrode following 50 minutes of electrolysis, measured following HEXS measurements, and used to scale HEXS intensity to film thickness. The inset shows a field of view imaging one of the ITO/GCA pores. The circle marks the area of enlargement shown on the right. Reprinted from ref. 159 with permission from IUCr.

Resolving amorphous domain edges as sites for redox activity and catalysis for transition metal oxyhydroxide OEC by PDF. A key challenge for catalysis research lies in resolving the sites and mechanisms for bond-making/bond-breaking catalysis. The role of the bulk lattice, metal-bridging oxygen sites for OEC in transition metal oxides has been described, particularly for highly covalent oxides.¹⁰⁴ However, for the late first-row transition metal oxyhydroxides, a large body of research including electrochemical metal K-edge EXAFS,^{21, 58, 126} oxygen K-edge XAS,²¹ electrochemical metal K-edge RIXS,¹¹⁸ magnetic resonance,¹⁶⁰⁻¹⁶² electrochemical analysis,^{19, 21, 22, 160, 163} time-resolved IR,⁴⁹ and isotope effects,^{20, 164, 165} has converged to identify high valence metal sites with terminal metal-oxo coordination at domain edges and defects as the most active sites for OEC. For the extensively investigated cobalt oxyhydroxides, mechanisms have focused on the role of edge-located di- μ -oxo-bridged Co(VI) atom pairs,^{19-21, 164, 165} illustrated in partial mechanistic scheme, Figure 12A.²⁰ A Co(IV-IV) oxidation state for the di- μ -oxo-bridged Co(VI) atom pair is understood to be the precursor to O-O bond formation that predominately occurs through direct intramolecular oxygen coupling (IMOC), either through the terminal oxyl atoms of the di- μ -oxo-bridged Co(VI) atom pair, site **a** in Figure 1B,²⁰ or through geminal oxygen coupling, site **b** in Figure 1B.^{21, 164, 166} A combined analysis of H/D isotope effects¹⁶⁵ and a comparative analysis of operando Co K-edge EXAFS and O K-edge XAS for a series of CoO_x materials with differing OEC efficiencies²¹ have resolved additional atomic structural factors linked to OEC function. A proposed expanded reaction scheme is shown in Figure 12B,¹⁶⁵ that now details the function of specific atomic sites in the individual proton-coupled electron transfer (PCET) redox steps which lead to OEC, and can be corroborated with

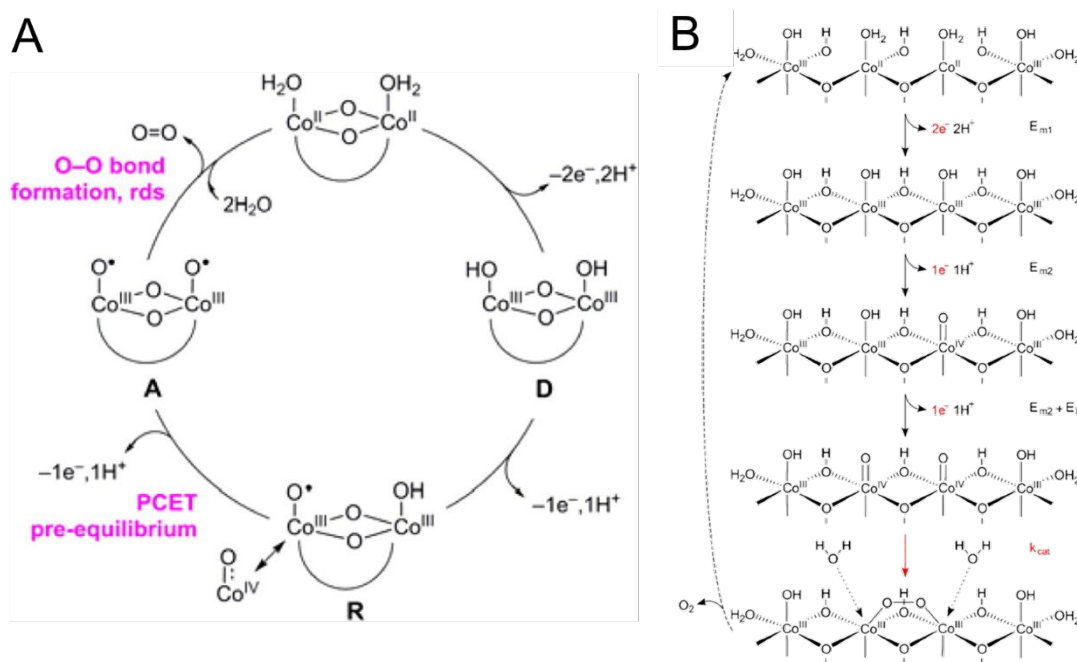


Figure 12. Reaction schemes for OEC in cobalt oxyhydroxides. **Part A** shows a reaction scheme for OEC illustrating PCET redox steps and charge accumulation in di- μ -oxo linked cobalt atoms, with the Co(IV)-Co(IV) state serving as the precursor for O-O bond formation. The curved connectors represent phosphate, or OH_x, terminal or bridging ligands. Reproduced with permission from ref 20. Copyright 2016 American Chemical Society. **Part B** shows an elaborated reaction scheme, illustrating specific protonation sites, metal coordination changes, and water nucleophilic attack to the Co(IV)-Co(IV) precursor state to generate O₂. Reproduced with permission from ref 165. Copyright 2019 American Chemical Society.

atomic density functional theory, DFT.¹⁶⁵ These analyses identify key differences in the functional reactivities of lattice μ_3 -oxo-bridge and edge μ_2 -oxo-bridge oxygen atom sites.^{21, 165} The models predict the special reactivity of the edge μ_2 -oxygen atoms for redox-linked protonation, and the coordination changes that are expected to accompany the catalytic cycle and occur at the μ_2 -oxygen atom sites.^{21, 165}

These studies demonstrate the critical impact that advanced X-ray spectroscopy analyses have on the resolution of OEC function. However, X-ray spectroscopy does not detect structure directly, but infers structure based on measured shifts in energies and intensities for X-ray transitions, and by comparison to computation and model structures. Following from this, it can be anticipated that enhancement in the resolution of mechanisms for OEC function could be achieved by combining X-ray spectroscopy analyses with X-ray structure measurements that are capable of resolving the locations for coordination changes that are expected accompany the catalytic cycle.

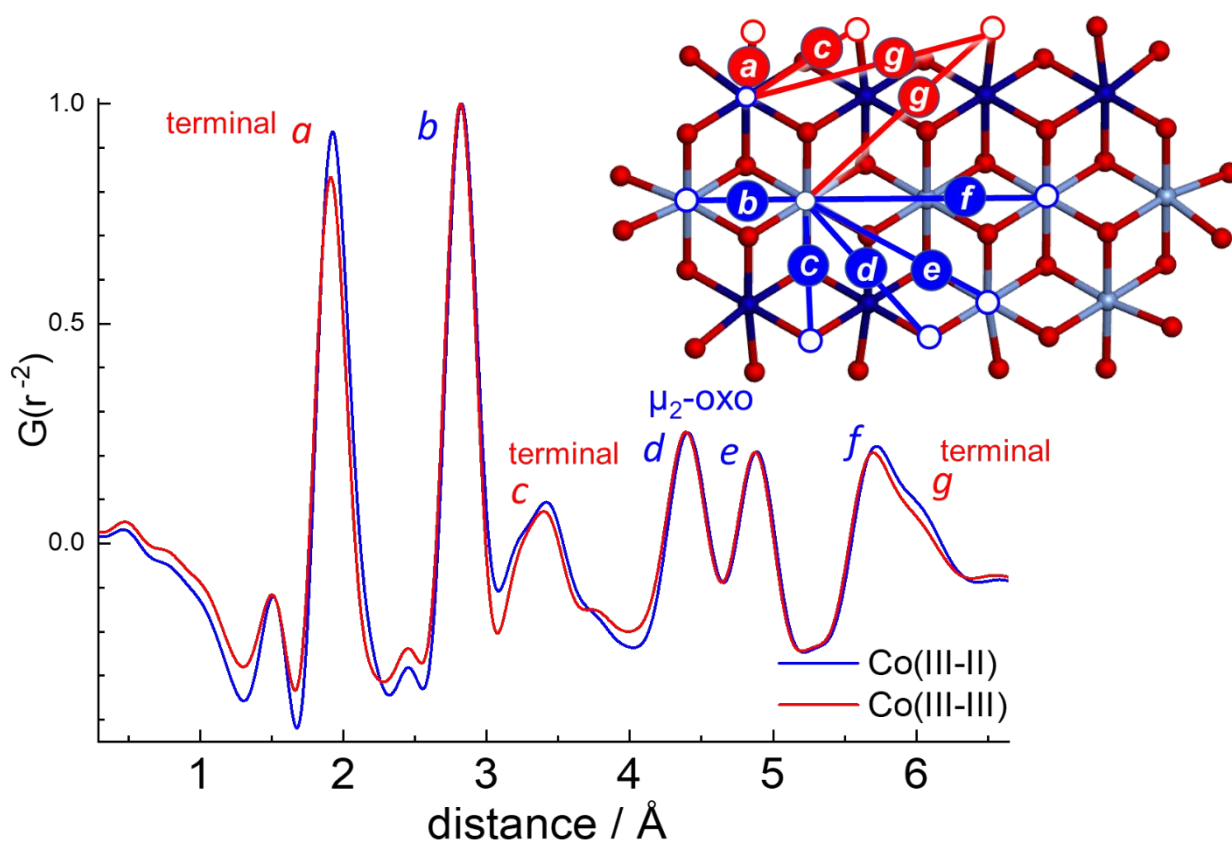


Figure 9. Electrochemical PDF fine structure change for CoO_x -Pi OEC films. The PDF patterns were recorded with the CoO_x -Pi OEC electrochemically poised in the Co(III-II) and Co(III-III) redox states, blue and red line traces, respectively. The inset shows the CoO_x -Pi domain structure model,²⁵ annotated with arrows showing how PDF peak distances correspond to locations in the domain structure. Co-O atom pairs involving the terminal oxygen ligand atoms are marked with red arrows a, c, g, while Co-O atom pairs involving di- μ -oxo-bridged oxygen at the domain edge are marked in blue, c, d. Selected non-terminal Co-Co atom pairs, b and f, are also marked in blue. Electrochemical PDF measurements show that peaks having contributions from atom pairs with the terminal oxygen ligand have redox state dependent changing in intensity, suggestive configurational broadening. PDF data were adapted from ref. 159 with permission from IUCr.

PDF analyses may offer an opportunity to distinguish sites for chemical reactivity. For example, PDF patterns for few-atom metal clusters contain information on pair distances for sites within the cluster. Figure 13 shows operando PDF patterns for the amorphous CoO_x -Pi thin-film oxygen-evolving catalyst, measured using the 3D porous working electrode assembly described above, Figure 11, and shown for films poised at electrochemical potentials corresponding to the Co(III-II) and Co(III-III) oxidation states.¹⁵⁹ Prior electrochemical Co K-edge EXAFS has shown that only a portion of the cobalt atoms undergo reversible Co(III/II) redox cycles.²¹ The interior lattice cobalt sites with μ_3 -oxo-ligation are inferred to be “irreducible”, or resistant to reduction to Co(II).²¹ The PDF shows that oxidation of the CoO_x -Pi film from the Co(II)-Co(III) oxidation is associated with the shortening of the coordinating Co-O bond distance in accord with redox dependent changes measured by EXAFS.⁵⁸ These PDF fine structure changes are fully reversible and can be cycled back and forth.¹⁵⁹ A notable feature of the redox PDF fine structure change is the amplitude attenuation seen for the coordinating Co-O bond distance peak, labeled **a**. The analysis shown in Figure 8 demonstrates how attenuation of PDF peak amplitudes can arise from dispersion in coordination geometry.^{25, 159} In the cobaltate domain model, the terminal oxo and domain edge μ_2 -oxo-bridge oxygen atoms make specific contributions to peaks in the PDF. The terminal oxygen atoms contribute to the Co-O atom pair peaks **a**, **c**, **g**, as indicated in the inset model, while the μ_2 -oxo-bridge oxygen atoms at the domain edge make contributions to the Co-O pair distance peaks **c**, **d**, **e**. Significantly, the oxidation-induced broadening and amplitude loss is seen for the set of the peaks **a**, **c**, **g** where the terminal oxo atoms make contributions, but not for the peaks **b**, **d**, **e**, **f**, where the μ_3 -oxo-bridge oxygen atoms make contributions. This result provides a spatially resolved identification that the terminal oxo ligands at domain edge cobalt atoms undergo Co(III/II) redox state change, and that the oxidation state change is correlated with a distortion in the coordination geometry for this oxygen ligand.¹⁵⁹ Within the context of the reaction scheme shown in Figure 12B,¹⁶⁵ it is also notable that the atom pair peaks associated with the μ_2 -oxo-bridge oxygen atom sites show no redox dependent changes and suggests that redox cycling does not distort the coordination geometry at this oxygen ligand site.

Work on resolving CoO_x -Pi redox state PDF fine structure changes is on-going. The present results suggest opportunities to exploit electrochemical PDF fine structure analyses as a site-discriminating approach¹⁵⁹ that can be combined with X-ray spectroscopy for a more discriminating, detailed examination of mechanistic models. We comment further that atom site identification from PDF fine structure changes is likely to be best implemented with molecular or few atom clusters. For example, the relatively smaller size and a higher proportion of domain edge to interior lattice sites for CoO_x -Pi compared to CoO_x -MePi and CoO_x -borate,^{28, 29} make the CoO_x -Pi OEC well-suited for to the effects of domain edge site structure.

3. Concluding Remarks and Prospects for Future Work.

This minireview has discussed examples showing how advances in soft and tender X-ray absorption and related hard X-ray emission spectroscopies have provided approaches for directly interrogating electronic configurations of transition metal catalysts with high resolution. Of particular impact is the ability to detect distinguishable electronic environments for both metal and coordinating ligand atom sets in complex materials. In the examples discussed, these capabilities have allowed specific electronic configurations and orbital structures to be linked to catalytic activity. At the opposite end of the X-ray spectrum, advances in high energy X-ray light sources, beamlines, and reciprocal space scattering techniques are emerging to demonstrate new opportunities for direct structure characterization of amorphous and disordered interfacial materials under operando conditions. Emerging work on interfacial, molecular and few atom cluster catalysts is demonstrating opportunities to resolve the atom pair distance

distributions that probe outer sphere coordination geometries with site-specific, spatially-resolved structures that are not otherwise accessible. Taken together, high-resolution spectroscopy and scattering approaches offer opportunities to achieve a more complete description of electronic and atomic structures underlying fundamental catalytic function.

Time-resolved X-ray spectroscopy and high energy X-ray scattering. Looking forward, clear opportunities and research priorities in catalysis lie in the tracking of the time evolution of electronic and nuclear structures along the reaction coordinate leading to bond-making and bond-breaking catalysis.¹⁶⁷⁻¹⁷¹ For multi-electron, proton-coupled water-splitting and fuels catalysis, the time-domain of interest spans from ultrafast timescales, associated with light-driven, excited state photochemistry, to microsecond and longer time domains that probe intermediate redox state advancement and charge-accumulating events and that precede bond-making and bond-breaking catalysis. The remarkable success in structure resolution of intermediate redox states leading to photosynthetic water-splitting by the $\text{Mn}_4\text{O}_5\text{Ca}$ OEC cluster in photosynthesis serves as a paradigm for the successful tracking multi-step catalysis driven by single electron charge-transfer events.¹⁷²⁻¹⁷⁶ A key challenge in artificial photosynthesis and fuels catalysis lies in creating (photo)electrochemical interfaces capable of comparably driving multi-step catalysis driven by single-electron redox steps.

Approaches for carrying out time-resolved electronic structure analyses by time-resolved soft XAS are well-advanced. X-ray free electron laser(XFEL)^{177, 178 73, 179-181 70} and high harmonic generation¹⁸² light source developments have created dramatic opportunities to track structural dynamics in light-excited states with ultrafast time resolution, and to probe structures for longer-lived intermediate states that are free of radiation damage.⁷² Opportunities for carrying out time-resolved HEXS lag behind those in place for soft, tender, and hard XAS, due in large part to the limited brightness in the high-energy X-ray region with current X-ray light sources. However the advent of new, fourth-generation light sources will create opportunities for time-resolved HEXS and PDF analyses. For example, upgrades to the Advanced Photon Source to a fourth-generation high energy synchrotron, will offer high energy X-ray beams (60 – 120 keV) with at least 2 orders of magnitude higher intensity and coherence.⁷¹ This will enable opportunities for the development of pump-probe PDF analyses with time resolution from sub-nanosecond to longer time domains. Further, high energy upgrades are possible for the Linear Coherent Linac Light Source (LCLS-II-HE), to extend the XFEL for 25 keV X-ray pulse analyses.⁷³ Pump-probe synchrotron time-resolved wide angle X-ray scattering using 25 keV X-rays have demonstrated that the increased reciprocal space resolution provided by this high-energy extension will be significant for deciphering outer sphere structural dynamics in excited state photochemistry.¹⁸³

Combined soft X-ray spectroscopy and high-energy X-ray scattering analyses for interfacial catalysts. Opportunities for further impact in the resolution of fundamental mechanisms in multi-step catalysis emerge from advances in X-ray light sources and surface synthesis, particularly those that offer new approaches for the interrogation of interfacial thin film and surface-supported molecular architectures under operando conditions. Notably, the coherent, diffraction-limited fourth generation synchrotrons will offer high energy X-ray beams (> 50 keV) for PDF analysis with submicron focused beams.^{71, 184} This will dramatically improve capabilities for the interrogation of interfacial ultra-thin films and supported metal clusters through both grazing incidence and focused beam techniques. In addition, advances in scaffold and electrochemically active surface synthesis techniques that allow X-ray data acquisition to be optimized for the same electrode-supported catalyst architecture using both soft and high energy X-ray regions will enable a combined electronic and atomic structure characterization of functional interfaces.

This will enable new opportunities to achieve an experimental characterization of the details of electronic and atomic structures that support interfacial catalysis. Particularly for amorphous materials and molecular complexes bound to solid surfaces where active site structures are typically only incompletely defined, these combined approaches will offer opportunities to achieve a more complete interrogation of electronic and atomic structures that support interfacial catalysis.

Acknowledgements

Work at Argonne National Laboratory on water-splitting catalysis was supported by the Division of Chemical Sciences, Geosciences, and Biosciences, Solar Photochemistry Program, Office of Basic Energy Sciences of the U.S. Department of Energy under Contract DE-AC02-06CH11357. Work on the X-ray analysis of sequential infiltration synthesis of metal oxides was supported as part of the Center for Advanced Materials for Energy-Water Systems (AMEWS), an Energy Frontier Research Center funded by the U.S. Department of Energy (DOE), Office of Science, Basic Energy Sciences (BES). High energy X-ray scattering measurements were carried out at beamline 11-ID-B of the Advanced Photon Source, an Office of Science User Facility operated for the U.S. Department of Energy (DOE) Office of Science by Argonne National Laboratory and supported by the U.S. DOE under Contract No. DE-AC02-06CH11357. Research at beamline 28-ID-1 of the National Synchrotron Light Source II was supported by U.S. Department of Energy (DOE) Office of Science User Facility operated for the DOE Office of Science by Brookhaven National Laboratory under Contract No. DE-SC0012704.

References

1. Y. He, T. Hamann and D. Wang, *Chemical Society Reviews*, 2019, **48**, 2182-2215.
2. F. Niu, D. Wang, F. Li, Y. Liu, S. Shen and T. J. Meyer, *Adv. Energy Mater.*, 2019, , 1900399.
3. T. R. Cook, D. K. Dogutan, S. Y. Reece, Y. Surendranath, T. S. Teets and D. G. Nocera, *Chemical Reviews*, 2010, **110**, 6474-6502.
4. M. Crespo-Quesada and E. Reisner, *Energy Environ. Sci.*, 2017, **10**, 1116-1127.
5. B. Zhang and L. Sun, *Chemical Society Reviews*, 2019, **48**, 2216-2264.
6. J. Su and L. Vayssieres, *ACS Energy Letters*, 2016, **1**, 121-135.
7. J. Timoshenko and A. I. Frenkel, *ACS Catal.*, 2019, **9**, 10192-10211.
8. M. Filez, E. A. Redekop, J. Dendooven, R. K. Ramachandran, E. Solano, U. Olsbye, B. M. Weckhuysen, V. V. Galvita, H. Poelman, C. Detavernier and G. B. Marin, *Angew. Chem. Int. Ed.*, 2019, **58**, 13220-13230.
9. A. J. Medford, M. R. Kunz, S. M. Ewing, T. Borders and R. Fushimi, *ACS Catal.*, 2018, **8**, 7403-7429.
10. A. Indra, P. W. Menezes, N. R. Sahraie, A. Bergmann, C. Das, M. Tallarida, D. Schmeisser, P. Strasser and M. Driess, *J. Amer. Chem. Soc.*, 2014, **136**, 17530-17536.
11. W. D. Chemelewski, H. C. Lee, J. F. Lin, A. J. Bard and C. B. Mullins, *J. Amer. Chem. Soc.*, 2014, **136**, 2843-2850.
12. A. Bergmann, E. Martinez-Moreno, D. Teschner, P. Chernev, M. Gliech, J. F. de Araújo, T. Reier, H. Dau and P. Strasser, *Nature Communications*, 2015, **6**, 8625.

13. M. S. Burke, L. J. Enman, A. S. Batchellor, S. H. Zou and S. W. Boettcher, *Chemistry of Materials*, 2015, **27**, 7549-7558.
14. D. González-Flores, I. Sánchez, I. Zaharieva, K. Klingan, J. Heidkamp, P. Chernev, P. W. Menezes, M. Driess, H. Dau and M. L. Montero, *Angewandte Chemie International Edition*, 2015, **54**, 2472-2476.
15. B. R. Goldsmith, B. Peters, J. K. Johnson, B. C. Gates and S. L. Scott, *ACS Catal.*, 2017, **7**, 7543-7557.
16. R. D. L. Smith, M. S. Prevot, R. D. Fagan, Z. P. Zhang, P. A. Sedach, M. K. J. Siu, S. Trudel and C. P. Berlinguette, *Science*, 2013, **340**, 60-63.
17. S. Anantharaj and S. Noda, 2020, **16**, 1905779.
18. T. A. Betley, Q. Wu, T. Van Voorhis and D. G. Nocera, *Inorganic Chemistry*, 2008, **47**, 1849-1861.
19. Y. Surendranath, M. W. Kanan and D. G. Nocera, *J. Am. Chem. Soc.*, 2010, **132**, 16501-16509.
20. A. M. Ullman, C. N. Brodsky, N. Li, S.-L. Zheng and D. G. Nocera, *J. Amer. Chem. Soc.*, 2016, **138**, 4229-4236.
21. A. Bergmann, T. E. Jones, E. Martinez Moreno, D. Teschner, P. Chernev, M. Gliech, T. Reier, H. Dau and P. Strasser, *Nature Catalysis*, 2018, **1**, 711-719.
22. M. B. Stevens, L. J. Enman, E. H. Korkus, J. Zaffran, C. D. M. Trang, J. Asbury, M. G. Kast, M. C. Toroker and S. W. Boettcher, *Nano Research*, 2019, **12**, 2288-2295.
23. M. B. Stevens, C. D. M. Trang, L. J. Enman, J. Deng and S. W. Boettcher, *J. Amer. Chem. Soc.*, 2017, **139**, 11361-11364.
24. M. W. Kanan, J. Yano, Y. Surendranath, M. Dinca, V. K. Yachandra and D. G. Nocera, *J. Am. Chem. Soc.*, 2010, **132**, 13692-13701.
25. D. Du, O. Kokhan, K. W. Chapman, P. J. Chupas and D. M. Tiede, *J. Am. Chem. Soc.*, 2012, **134**, 11096-11099.
26. J. Huang, J. D. Blakemore, D. Fazi, O. Kokhan, N. D. Schley, R. H. Crabtree, G. W. Brudvig and D. M. Tiede, *Phys. Chem. Chem. Phys.*, 2014, **16**, 1814-1819.
27. J. A. Kurzman, K. E. Dettelbach, A. J. Martinolich, C. P. Berlinguette and J. R. Neilson, *Chemistry of Materials*, 2015, **27**, 3462-3470.
28. C. L. Farrow, D. K. Bediako, Y. Surendranath, D. G. Nocera and S. J. L. Billinge, *J. Am. Chem. Soc.*, 2013, **135**, 6403-6406.
29. G. Kwon, O. Kokhan, A. Han, K. W. Chapman, P. J. Chupas, P. Du and D. M. Tiede, *Acta Crystallogr.*, 2015, **B71**, 713-721.
30. A. S. Batchellor, G. Kwon, F. A. L. Laskowski, D. M. Tiede and S. W. Boettcher, *Journal of Physical Chemistry C*, 2017, **121**, 25421-25429.
31. D. K. Bediako, C. Costentin, E. C. Jones, D. G. Nocera and J.-M. Savéant, *J. Amer. Chem. Soc.*, 2013, **135**, 10492-10502.
32. K. Klingan, F. Ringleb, I. Zaharieva, J. Heidkamp, P. Chernev, D. Gonzalez-Flores, M. Risch, A. Fischer and H. Dau, *ChemSusChem*, 2014, **7**, 1301-1310.
33. C. N. Brodsky, D. K. Bediako, C. Shi, T. P. Keane, C. Costentin, S. J. L. Billinge and D. G. Nocera, *ACS Applied Energy Materials*, 2019, **2**, 3-12.
34. J. Qiu, H. Hajibabaei, M. R. Nellist, F. A. L. Laskowski, S. Z. Oener, T. W. Hamann and S. W. Boettcher, *ACS Energy Letters*, 2018, **3**, 961-969.
35. G. Kwon, H. Jang, J.-S. Lee, A. Mane, D. J. Mandia, S. R. Soltau, L. M. Utschig, A. B. F. Martinson, D. M. Tiede, H. Kim and J. Kim, *J. Amer. Chem. Soc.*, 2018, **140**, 10710-10720.
36. T. J. Meyer, M. V. Sheridan and B. D. Sherman, *Chemical Society Reviews*, 2017, **46**, 6148-6169.
37. M. D. Karkas and B. Akerman, *Dalton Transactions*, 2016, **45**, 14421-14461.
38. X. Ding, L. Zhang, Y. Wang, A. Liu and Y. Gao, *Coordination Chemistry Reviews*, 2018, **357**, 130-143.

39. S. Berardi, S. Drouet, L. Francàs, C. Gimbert-Suriñach, M. Guttentag, C. Richmond, T. Stoll and A. Llobet, *Chemical Society Reviews*, 2014, **43**, 7501-7519.
40. W. Li, D. He, S. W. Sheehan, Y. M. He, J. E. Thorne, X. H. Yao, G. W. Brudvig and D. W. Wang, *Energy Environ. Sci.*, 2016, **9**, 1794-1802.
41. P. Xu, N. S. McCool and T. E. Mallouk, *Nano Today*, 2017, **14**, 42-58.
42. P. Garrido-Barros, R. Matheu, C. Gimbert-Suriñach and A. Llobet, *Current Opinion in Electrochemistry*, 2019, **15**, 140-147.
43. W. Kim, E. Edri and H. Frei, *Accounts of Chemical Research*, 2016, **49**, 1634-1645.
44. S. W. Sheehan, J. M. Thomsen, U. Hintermair, R. H. Crabtree, G. W. Brudvig and C. A. Schmuttenmaer, *Nature Communications*, 2015, **6**, 6469.
45. Y. Zhao, K. R. Yang, Z. Wang, X. Yan, S. Cao, Y. Ye, Q. Dong, X. Zhang, J. E. Thorne, L. Jin, K. L. Materna, A. Trimpalis, H. Bai, S. C. Fakra, X. Zhong, P. Wang, X. Pan, J. Guo, M. Flytzani-Stephanopoulos, G. W. Brudvig, V. S. Batista and D. Wang, *Proceedings of the National Academy of Sciences*, 2018, **115**, 2902-2907.
46. Y. Zhao, X. Yan, K. R. Yang, S. Cao, Q. Dong, J. E. Thorne, K. L. Materna, S. Zhu, X. Pan, M. Flytzani-Stephanopoulos, G. W. Brudvig, V. S. Batista and D. Wang, *ACS Central Science*, 2018, **4**, 1166-1172.
47. H. F. Liu and H. Frei, *ACS Catal.*, 2020, **10**, 2138-2147.
48. M. Zhang and H. Frei, in *Annual Review of Physical Chemistry, Vol 68*, eds. M. A. Johnson and T. J. Martinez, Annual Reviews, Palo Alto, 2017, vol. 68, pp. 209-231.
49. M. Zhang, M. de Respinis and H. Frei, *Nat Chem*, 2014, **6**, 362-367.
50. X. H. Chen, S. N. Choing, D. J. Aschaffenburg, C. D. Pemmaraju, D. Prendergast and T. Cuk, *J. Amer. Chem. Soc.*, 2017, **139**, 1830-1841.
51. D. M. Herlihy, M. M. Waegle, X. H. Chen, C. D. Pemmaraju, D. Prendergast and T. Cuk, *Nat. Chem.*, 2016, **8**, 549-555.
52. D. Lebedev, Y. Pineda-Galvan, Y. Tokimaru, A. Fedorov, N. Kaeffer, C. Coperet and Y. Pushkar, *J. Amer. Chem. Soc.*, 2018, **140**, 451-458.
53. Y. Gorlin, B. Lassalle-Kaiser, J. D. Benck, S. Gul, S. M. Webb, V. K. Yachandra, J. Yano and T. F. Jaramillo, *J. Amer. Chem. Soc.*, 2013, **135**, 8525-8534.
54. R. Chatterjee, C. Weninger, A. Loukianov, S. Gul, F. D. Fuller, M. H. Cheah, T. Fransson, C. C. Pham, S. Nelson, S. Song, A. Britz, J. Messinger, U. Bergmann, R. Alonso-Mori, V. K. Yachandra, J. Kern and J. Yano, *J. Synchrot. Radiat.*, 2019, **26**, 1716-1724.
55. D. Drevon, M. Görlin, P. Chernev, L. Xi, H. Dau and K. M. Lange, *Scientific Reports*, 2019, **9**, 1532.
56. S. Bordiga, E. Groppo, G. Agostini, J. A. van Bokhoven and C. Lamberti, *Chemical Reviews*, 2013, **113**, 1736-1850.
57. C. H. M. van Oversteeg, H. Q. Doan, F. M. F. de Groot and T. Cuk, *Chemical Society Reviews*, 2017, **46**, 102-125.
58. M. Risch, F. Ringleb, M. Kohlhoff, P. Bogdanoff, P. Chernev, I. Zaharieva and H. Dau, *Energy Environ. Sci.*, 2015, **8**, 661-674.
59. M. J. Zachman, J. A. Hachtel, J. C. Idrobo and M. Chi, *Angew. Chem. Int. Ed.*, 2020, **59**, 1384-1396.
60. F. Reikowski, F. Maroun, I. Pacheco, T. Wiegmann, P. Allongue, J. Stettner and O. M. Magnussen, *ACS Catal.*, 2019, **9**, 3811-3821.
61. V. Streibel, M. Hävecker, Y. Yi, J. J. Velasco Vélez, K. Skorupska, E. Stotz, A. Knop-Gericke, R. Schlögl and R. Arrigo, *Topics in Catalysis*, 2018, **61**, 2064-2084.
62. S. Axnanda, E. J. Crumlin, B. Mao, S. Rani, R. Chang, P. G. Karlsson, M. O. M. Edwards, M. Lundqvist, R. Moberg, P. Ross, Z. Hussain and Z. Liu, *Scientific Reports*, 2015, **5**, 9788.

63. M. Favaro, W. S. Drisdell, M. A. Marcus, J. M. Gregoire, E. J. Crumlin, J. A. Haber and J. Yano, *ACS Catal.*, 2017, **7**, 1248-1258.
64. M. Favaro, J. H. Yang, S. Nappini, E. Magnano, F. M. Toma, E. J. Crumlin, J. Yano and I. D. Sharp, *J. Amer. Chem. Soc.*, 2017, **139**, 8960-8970.
65. E. A. Carbonio, J.-J. Velasco-Velez, R. Schlögl and A. Knop-Gericke, *Journal of The Electrochemical Society*, 2020, **167**, 054509.
66. M. V. Varsha and G. Nageswaran, *Frontiers in Chemistry*, 2020, **8**.
67. J. Li, R. Güttinger, R. Moré, F. Song, W. Wan and G. R. Patzke, *Chemical Society Reviews*, 2017, **46**, 6124-6147.
68. M. K. Samantaray, V. D'Elia, E. Pump, L. Falivene, M. Harb, S. Ould Chikh, L. Cavallo and J.-M. Basset, *Chemical Reviews*, 2020, **120**, 734-813.
69. E. Fabbri, D. F. Abbott, M. Nachttegaal and T. J. Schmidt, *Current Opinion in Electrochemistry*, 2017, **5**, 20-26.
70. K. Asakura, K. J. Gaffney, C. Milne and M. Yabashi, *Physical Chemistry Chemical Physics*, 2020, **22**, 2612-2614.
71. M. Borland, V. Sajaev and Y. Sun, presented in part at the Proc. 6th International Particle Accelerator Conference (IPAC'15), Richmond, VA, USA, May 3-8, 2015, 2015.
72. R. Neutze, R. Wouts, D. van der Spoel, E. Weckert and J. Hajdu, *Nature*, 2000, **406**, 752-757.
73. R. W. Schoenlein, S. Boutet, M. P. Minitti and A. M. Dunne, *Appl. Sci.-Basel*, 2017, **7**, 20.
74. Z. W. Seh, J. Kibsgaard, C. F. Dickens, I. B. Chorkendorff, J. K. Norskov and T. F. Jaramillo, *Science*, 2017, **355**, 1.
75. J. K. Nørskov, F. Abild-Pedersen, F. Studt and T. Bligaard, *Proceedings of the National Academy of Sciences of the United States of America*, 2011, **108**, 937-943.
76. Y. Zheng, Y. Jiao, M. Jaroniec and S. Z. Qiao, *Angew. Chem.-Int. Edit.*, 2015, **54**, 52-65.
77. L. Xi, P. D. Tran, S. Y. Chiam, P. S. Bassi, W. F. Mak, H. K. Mulmudi, S. K. Batabyal, J. Barber, J. S. C. Loo and L. H. Wong, *The Journal of Physical Chemistry C*, 2012, **116**, 13884-13889.
78. L. Xi and K. M. Lange, *Catalysts*, 2018, **8**, 497.
79. A. S. M. Ismail, Y. Uemura, S. H. Park, S. Kwon, M. Kim, H. Elnaggar, F. Frati, Y. Niwa, H. Wadati, Y. Hirata, Y. Zhang, K. Yamagami, S. Yamamoto, I. Matsuda, U. Halisdemir, G. Koster, B. M. Weckhuysen and F. M. F. de Groot, *Physical Chemistry Chemical Physics*, 2020, **22**, 2685-2692.
80. A. A. Cordones, J. H. Lee, K. Hong, H. Cho, K. Garg, M. Boggio-Pasqua, J. J. Rack, N. Huse, R. W. Schoenlein and T. K. Kim, *Nature Communications*, 2018, **9**, 9.
81. S. Biswas, J. Husek, S. Londo and L. R. Baker, *Nano Letters*, 2018, **18**, 1228-1233.
82. M. Ochmann, I. von Ahnen, A. A. Cordones, A. Hussain, J. H. Lee, K. Hong, K. Adamczyk, O. Vendrell, T. K. Kim, R. W. Schoenlein and N. Huse, *J. Amer. Chem. Soc.*, 2017, **139**, 4797-4804.
83. S. Koroidov, K. Hong, K. S. Kjaer, L. Li, K. Kunnus, M. Reinhard, R. W. Hartsock, D. Amit, R. Eisenberg, C. Das Pemmaraju, K. J. Gaffney and A. A. Cordones, *Inorganic Chemistry*, 2018, **57**, 13167-13175.
84. J. Stohr, *Springer Series in Surface Science*, 1992, **25**, 122.
85. A. Kuznetsova, I. Popova, J. T. Yates, M. J. Bronikowski, C. B. Huffman, J. Liu, R. E. Smalley, H. H. Hwu and J. G. Chen, *J. Amer. Chem. Soc.*, 2001, **123**, 10699-10704.
86. K. Kim, P. Zhu, N. Li, X. Ma and Y. Chen, *Carbon*, 2011, **49**, 1745-1751.
87. F. M. F. de Groot, M. Grioni, J. C. Fuggle, J. Ghijsen, G. A. Sawatzky and H. Petersen, *Physical Review B*, 1989, **40**, 5715-5723.
88. M. Salluzzo and G. Ghiringhelli, in *Spectroscopy of Complex Oxide Interfaces: Photoemission and Related Spectroscopies*, eds. C. Cancellieri and V. N. Strocov, Springer International Publishing, Cham, 2018, DOI: 10.1007/978-3-319-74989-1_11, pp. 283-314.

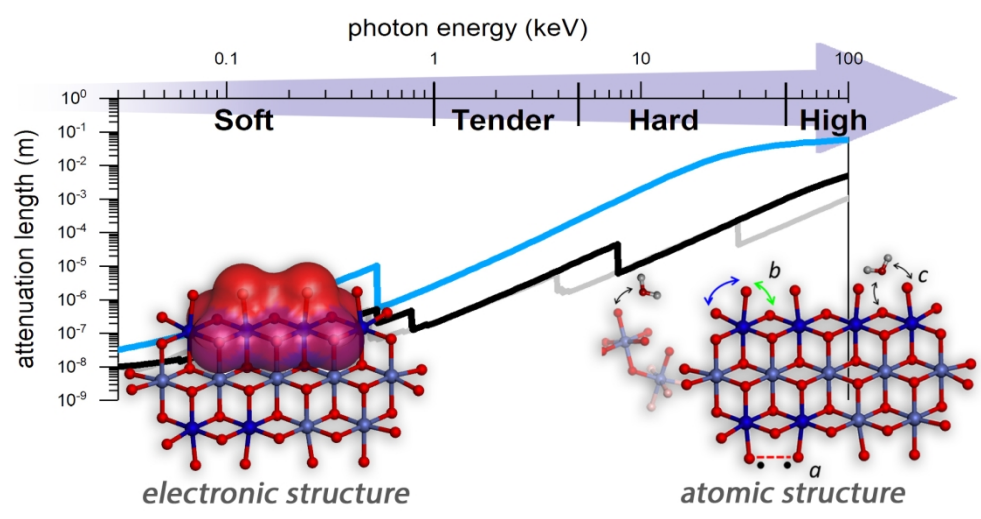
89. M. Kubin, M. Guo, T. Kroll, H. Löchel, E. Källman, M. L. Baker, R. Mitzner, S. Gul, J. Kern, A. Föhlisch, A. Erko, U. Bergmann, V. Yachandra, J. Yano, M. Lundberg and P. Wernet, *Chem. Sci.*, 2018, **9**, 6813-6829.
90. T. J. Regan, H. Ohldag, C. Stamm, F. Nolting, J. Luning, J. Stohr and R. L. White, *Physical Review B*, 2001, **64**, 11.
91. W. S. Yoon, K. B. Kim, M. G. Kim, M. K. Lee, H. J. Shin, J. M. Lee, J. S. Lee and C. H. Yo, *Journal of Physical Chemistry B*, 2002, **106**, 2526-2532.
92. I. Josefsson, K. Kunnus, S. Schreck, A. Föhlisch, F. de Groot, P. Wernet and M. Odelius, *J. Phys. Chem. Lett.*, 2012, **3**, 3565-3570.
93. F. de Groot, *Coordination Chemistry Reviews*, 2005, **249**, 31-63.
94. M. L. Baker, M. W. Mara, J. J. Yan, K. O. Hodgson, B. Hedman and E. I. Solomon, *Coordination Chemistry Reviews*, 2017, **345**, 182-208.
95. M. M. van Schooneveld and S. DeBeer, *Journal of Electron Spectroscopy and Related Phenomena*, 2015, **198**, 31-56.
96. L. J. P. Ament, M. van Veenendaal, T. P. Devereaux, J. P. Hill and J. van den Brink, *Reviews of Modern Physics*, 2011, **83**, 705-767.
97. S. N. MacMillan and K. M. Lancaster, *ACS Catal.*, 2017, **7**, 1776-1791.
98. T. Kroll, C. Weninger, R. Alonso-Mori, D. Sokaras, D. L. Zhu, L. Mercadier, V. P. Majety, A. Marinelli, A. Lutman, M. W. Guetg, F. J. Decker, S. Boutet, A. Aquila, J. Koglin, J. Koralek, D. P. DePonte, J. Kern, F. D. Fuller, E. Pastor, T. Fransson, Y. Zhang, J. Yano, V. K. Yachandra, N. Rohringer and U. Bergmann, *Physical Review Letters*, 2018, **120**, 6.
99. M. Kubin, J. Kern, S. Gul, T. Kroll, R. Chatterjee, H. Lochel, F. D. Fuller, R. G. Sierra, W. Quevedo, C. Weninger, J. Rehanek, A. Firsov, H. Laksmono, C. Weninger, R. Alonso-Mori, D. L. Nordlund, B. Lassalle-Kaiser, J. M. Glowina, J. Krzywinski, S. Moeller, J. J. Turner, M. P. Minitti, G. L. Dakovski, S. Koroidov, A. Kawde, J. S. Kanady, E. Y. Tsui, S. Suseno, Z. J. Han, E. Hill, T. Taguchi, A. S. Borovik, T. Agapie, J. Messinger, A. Erko, A. Föhlisch, U. Bergmann, R. Mitzner, V. K. Yachandra, J. Yano and P. Wernet, *Struct. Dyn.-US*, 2017, **4**, 16.
100. G. Vankó, F. M. F. de Groot, S. Huotari, R. J. Cava, T. Lorenz and M. Reuther, Intersite 4p-3d hybridization in cobalt oxides: a resonant x-ray emission spectroscopy study, arXiv.org (0802.2744v1).
101. F. de Groot, *Chemical Reviews*, 2001, **101**, 1779-1808.
102. P. Glatzel, J. Yano, U. Bergmann, H. Visser, J. H. Robblee, W. W. Gu, F. M. F. de Groot, S. P. Cramer and V. K. Yachandra, *Journal of Physics and Chemistry of Solids*, 2005, **66**, 2163-2167.
103. J. Suntivich, K. J. May, H. A. Gasteiger, J. B. Goodenough and Y. Shao-Horn, *Science*, 2011, **334**, 1383-1385.
104. A. Grimaud, O. Diaz-Morales, B. Han, W. T. Hong, Y.-L. Lee, L. Giordano, K. A. Stoerzinger, M. T. M. Koper and Y. Shao-Horn, *Nat. Chem.*, 2017, **9**, 457-465.
105. J. Suntivich, W. T. Hong, Y.-L. Lee, J. M. Rondinelli, W. Yang, J. B. Goodenough, B. Dabrowski, J. W. Freeland and Y. Shao-Horn, *The Journal of Physical Chemistry C*, 2014, **118**, 1856-1863.
106. F. Song, L. Bai, A. Moysiadou, S. Lee, C. Hu, L. Liardet and X. Hu, *J. Amer. Chem. Soc.*, 2018, **140**, 7748-7759.
107. V. Pfeifer, T. E. Jones, J. J. Velasco Vélez, R. Arrigo, S. Piccinin, M. Hävecker, A. Knop-Gericke and R. Schlögl, *Chem. Sci.*, 2017, **8**, 2143-2149.
108. R. G. Hadt, D. Hayes, C. N. Brodsky, A. M. Ullman, D. M. Casa, M. H. Upton, D. G. Nocera and L. X. Chen, *J. Amer. Chem. Soc.*, 2016, **138**, 11017-11030.
109. Y. Surendranath, M. Dinca and D. G. Nocera, *J. Am. Chem. Soc.*, 2009, **131**, 2615-2650.
110. S. Y. Reece, J. A. Hamel, K. Sung, T. D. Jarvi, A. J. Esswein, J. J. H. Pijpers and D. G. Nocera, *Science*, 2011, **334**, 645-648.

111. M. Dinca, Y. Surendranath and D. G. Nocera, *Proceedings of the National Academy of Sciences of the United States of America*, 2010, **107**, 10337-10341.
112. A. J. Esswein, Y. Surendranath, S. Y. Reece and D. G. Nocera, *Energy & Environ. Sci.*, 2011, **4**, 499-504.
113. M. Risch, K. Klingan, F. Ringleb, P. Chernev, I. Zaharieva, A. Fischer and H. Dau, *ChemSusChem*, 2012, **5**, 542-549.
114. L. Trotochaud, S. L. Young, J. K. Ranney and S. W. Boettcher, *J. Am. Chem. Soc.*, 2014, **136**, 6744-6753.
115. D. G. Nocera, *Accounts of Chemical Research*, 2012, **45**, 767-776.
116. Y. Surendranath, D. A. Lutterman, Y. Liu and D. G. Nocera, *J. Am. Chem. Soc.*, 2012, **134**, 6326-6336.
117. F. Massel, S. Ahmadi, M. Hahlin, Y. S. Liu, J. H. Guo, T. Edvinsson, H. Rensmo and L. C. Duda, *Journal of Electron Spectroscopy and Related Phenomena*, 2018, **224**, 3-7.
118. D. Friebel, M. Bajdich, B. S. Yeo, M. W. Louie, D. J. Miller, H. Sanchez Casalongue, F. Mbuga, T.-C. Weng, D. Nordlund, D. Sokaras, R. Alonso-Mori, A. T. Bell and A. Nilsson, *Phys. Chem. Chem. Phys.*, 2013, **15**, 17460-17467.
119. M. Al Samarai, M. U. Delgado-Jaime, H. Ishii, N. Hiraoka, K.-D. Tsuei, J. P. Rueff, B. Lassale-Kaiser, B. M. Weckhuysen and F. M. F. de Groot, *The Journal of Physical Chemistry C*, 2016, **120**, 24063-24069.
120. Y. Ye, J. E. Thorne, C. H. Wu, Y.-S. Liu, C. Du, J.-W. Jang, E. Liu, D. Wang and J. Guo, *The Journal of Physical Chemistry B*, 2018, **122**, 927-932.
121. J. Guo, T. Tong, L. Svec, J. Go, C. Dong and J.-W. Chiou, *J Vac Sci Technol A*, 2007, **25**, 1231-1233.
122. D. K. Bora, P.-A. Glans, J. Pepper, Y.-S. Liu, C. Du, D. Wang and J.-H. Guo, *Rev. Sci. Instrum.*, 2014, **85**, 043106.
123. Y.-S. Liu, X. Feng, P.-A. Glans and J. Guo, *Solar Energy Materials and Solar Cells*, 2020, **208**, 110432.
124. D. Asakura, E. Hosono, H. Niwa, H. Kiuchi, J. Miyawaki, Y. Nanba, M. Okubo, H. Matsuda, H. Zhou, M. Oshima and Y. Harada, *Electrochemistry Communications*, 2015, **50**, 93-96.
125. D. Asakura, Y. Nanba, M. Okubo, H. Niwa, H. Kiuchi, J. Miyawaki, M. Oshima, E. Hosono and Y. Harada, *Physical Chemistry Chemical Physics*, 2019, **21**, 26351-26357.
126. M. Yoshida, Y. Mitsutomi, T. Mineo, M. Nagasaka, H. Yuzawa, N. Kosugi and H. Kondoh, *The Journal of Physical Chemistry C*, 2015, **119**, 19279-19286.
127. J. D. Koralek, J. B. Kim, P. Brůža, C. B. Curry, Z. Chen, H. A. Bechtel, A. A. Cordones, P. Sperling, S. Toleikis, J. F. Kern, S. P. Moeller, S. H. Glenzer and D. P. DePonte, *Nature Communications*, 2018, **9**, 1353.
128. R. González-Moreno, P. L. Cook, I. Zegkinoglou, X. Liu, P. S. Johnson, W. Yang, R. E. Ruther, R. J. Hamers, R. Tena-Zaera, F. J. Himpsel, J. E. Ortega and C. Rogero, *The Journal of Physical Chemistry C*, 2011, **115**, 18195-18201.
129. D. Wang, J. Zhou, Y. Hu, J. Yang, N. Han, Y. Li and T.-K. Sham, *The Journal of Physical Chemistry C*, 2015, **119**, 19573-19583.
130. T. Egami and S. J. L. Billinge, *Underneath The Bragg Peaks: Structural Analysis of Complex Materials*, Pergamon, Oxford, UK, 2012.
131. K. Laaziri, S. Kycia, S. Roorda, M. Chicoine, J. L. Robertson, J. Wang and S. C. Moss, *Physical Review B*, 1999, **60**, 13520-13533.
132. S. J. L. Billinge and M. G. Kanatzidis, *Chem. Commun.*, 2004, DOI: 10.1039/b309577k, 749-760.
133. S. J. L. Billinge, *Philosophical Transactions of the Royal Society A: Mathematical, Physical and Engineering Sciences*, 2019, **377**, 20180413.
134. Y. Ren and X. B. Zuo, *Small Methods*, 2018, **2**, 19.

135. M. A. Newton, *Catalysts*, 2017, **7**, 49.
136. K. L. Mulfort, A. Mukherjee, O. Kokhan, P. W. Du and D. M. Tiede, *Chem. Soc. Rev.*, 2013, **42**, 2215-2227.
137. C. Benmore, *ISRN Materials Science*, 2012, **2012**.
138. P. J. Chupas, K. W. Chapman, H. L. Chen and C. P. Grey, *Catal. Today*, 2009, **145**, 213-219.
139. V. Petkov, *Materials Today*, 2008, **11**, 28-38.
140. D. C. Koningsberger, B. L. Mojct, G. E. van Dorssen and D. E. Ramaker, *Topics in Catalysis*, 2000, **10**, 143-155.
141. J. E. Penner-Hahn, *Coordination Chemistry Reviews*, 1999, **190-192**, 1101-1123.
142. J. D. Blakemore, M. W. Mara, M. N. Kushner-Lenhoff, N. D. Schley, S. J. Konezny, I. Rivalta, C. F. A. Negre, R. C. Snoeberger, O. Kokhan, J. Huang, A. Stickrath, L. A. Tran, M. L. Parr, L. X. Chen, D. M. Tiede, V. S. Batista, R. H. Crabtree and G. W. Brudvig, *Inorg. Chem.*, 2013, **52**, 1860-1871.
143. K. R. Yang, A. J. Matula, G. Kwon, J. Hong, S. W. Sheehan, J. M. Thomsen, G. W. Brudvig, R. H. Crabtree, D. M. Tiede, L. X. Chen and V. S. Batista, *J. Amer. Chem. Soc.*, 2016, **138**, 5511-5514.
144. S. B. Sinha, D. Y. Shopov, L. S. Sharninghausen, C. J. Stein, B. Q. Mercado, D. Balcells, T. B. Pedersen, M. Reiher, G. W. Brudvig and R. H. Crabtree, *J. Amer. Chem. Soc.*, 2017, **139**, 9672-9683.
145. D. Y. Shopov, L. S. Sharninghausen, S. B. Sinha, B. Q. Mercado, D. Balcells, G. W. Brudvig and R. H. Crabtree, *Inorganic Chemistry*, 2018, **57**, 5684-5691.
146. X. He, R. Z. Waldman, D. J. Mandia, N. Jeon, N. J. Zaluzec, O. J. Borkiewicz, U. Ruett, S. B. Darling, A. B. F. Martinson and D. M. Tiede, *ACS Nano*, 2020, **submitted**.
147. C. Z. Leng and M. D. Losego, *Materials Horizons*, 2017, **4**, 747-771.
148. R. Z. Waldman, D. J. Mandia, A. Yanguas-Gil, A. B. F. Martinson, J. W. Elam and S. B. Darling, *The Journal of Chemical Physics*, 2019, **151**, 190901.
149. Q. Peng, Y.-C. Tseng, S. B. Darling and J. W. Elam, *Advanced Materials*, 2010, **22**, 5129-5133.
150. T. Segal-Peretz, J. Winterstein, M. Doxastakis, A. Ramírez-Hernández, M. Biswas, J. Ren, H. S. Suh, S. B. Darling, J. A. Liddle, J. W. Elam, J. J. de Pablo, N. J. Zaluzec and P. F. Nealey, *ACS Nano*, 2015, **9**, 5333-5347.
151. R. Z. Waldman, N. Jeon, D. J. Mandia, O. Heinonen, S. B. Darling and A. B. F. Martinson, *Chemistry of Materials*, 2019, **31**, 5274-5285.
152. A.-C. Dippel, M. Roelsgaard, U. Boettger, T. Schneller, O. Gutowski and U. Ruett, *IUCrJ*, 2019, **6**, 290-298.
153. V. Petkov, B. Prasai, S. Shan, Y. Ren, J. Wu, H. Cronk, J. Luo and C.-J. Zhong, *Nanoscale*, 2016, **8**, 10749-10767.
154. H. Jung, P. K. Allan, Y.-Y. Hu, O. J. Borkiewicz, X.-L. Wang, W.-Q. Han, L.-S. Du, C. J. Pickard, P. J. Chupas, K. W. Chapman, A. J. Morris and C. P. Grey, *Chemistry of Materials*, 2015, **27**, 1031-1041.
155. O. J. Borkiewicz, K. M. Wiaderek, P. J. Chupas and K. W. Chapman, *The Journal of Physical Chemistry Letters*, 2015, **6**, 2081-2085.
156. K. M. Wiaderek, O. J. Borkiewicz, E. Castillo-Martínez, R. Robert, N. Pereira, G. G. Amatucci, C. P. Grey, P. J. Chupas and K. W. Chapman, *J. Amer. Chem. Soc.*, 2013, **135**, 4070-4078.
157. O. J. Borkiewicz, B. Shyam, K. M. Wiaderek, C. Kurtz, P. J. Chupas and K. W. Chapman, *J. Appl. Crystallogr.*, 2012, **45**, 1261-1269.
158. M. J. Young, N. M. Bedford, N. Jiang, D. Lin and L. Dai, *J. Synchrotr. Radiat.*, 2017, **24**, 787-795.
159. G. Kwon, Y.-H. Cho, K.-B. Kim, J. D. Emery, I. S. Kim, X. Zhang, A. B. F. Martinson and D. M. Tiede, *J. Synchrotron Rad.*, 2019, **Volume 26 (5)**, 1600-1611.
160. J. B. Gerken, J. G. McAlpin, J. Y. C. Chen, M. L. Rigsby, W. H. Casey, R. D. Britt and S. S. Stahl, *J. Amer. Chem. Soc.*, 2011, **133**, 14431-14442.

161. J. G. McAlpin, Y. Surendranath, M. Dinca, T. A. Stich, S. A. Stoian, W. H. Casey, D. G. Nocera and R. D. Britt, *J. Am. Chem. Soc.*, 2010, **132**, 6882-6883.
162. R. I. Saylor, B. M. Hunter, W. Fu, H. B. Gray and R. D. Britt, *J. Amer. Chem. Soc.*, 2020, **142**, 1838-1845.
163. D. K. Bediako, A. M. Ullman and D. G. Nocera, in *Solar Energy for Fuels*, eds. H. Tüysüz and C. K. Chan, Springer International Publishing, Cham, 2016, DOI: 10.1007/128_2015_649, pp. 173-213.
164. S. Koroidov, M. F. Anderlund, S. Styring, A. Thapper and J. Messinger, *Energy Environ. Sci.*, 2015, **8**, 2492-2503.
165. C. Pasquini, I. Zaharieva, D. González-Flores, P. Chernev, M. R. Mohammadi, L. Guidoni, R. D. L. Smith and H. Dau, *J. Amer. Chem. Soc.*, 2019, **141**, 2938-2948.
166. G. Mattioli, P. Giannozzi, A. A. Bonapasta and L. Guidonili, *J. Amer. Chem. Soc.*, 2013, **135**, 15353-15363.
167. L. X. Chen, M. L. Shelby, P. J. Lestrangle, N. E. Jackson, K. Haldrup, M. W. Mara, A. B. Stickrath, D. L. Zhu, H. Lemke, M. Chollet, B. M. Hoffman and X. S. Li, *Faraday Discussions*, 2016, **194**, 639-658.
168. K. Kunnus, M. Vacher, T. C. B. Harlang, K. S. Kjær, K. Haldrup, E. Biasin, T. B. van Driel, M. Pápai, P. Chabera, Y. Liu, H. Tatsuno, C. Timm, E. Källman, M. Delcey, R. W. Hartsock, M. E. Reinhard, S. Koroidov, M. G. Laursen, F. B. Hansen, P. Vester, M. Christensen, L. Sandberg, Z. Németh, D. S. Szemes, É. Bajnóczi, R. Alonso-Mori, J. M. Glowina, S. Nelson, M. Sikorski, D. Sokaras, H. T. Lemke, S. E. Canton, K. B. Møller, M. M. Nielsen, G. Vankó, K. Wärnmark, V. Sundström, P. Persson, M. Lundberg, J. Uhlig and K. J. Gaffney, *Nature Communications*, 2020, **11**, 634.
169. Q. Kong, D. Khakhulin, I. A. Shkrob, J. H. Lee, X. Zhang, J. Kim, K. H. Kim, J. Jo, J. Kim, J. Kang, V.-T. Pham, G. Jennings, C. Kurtz, R. Spence, L. X. Chen, M. Wulff and H. Ihee, *Struct. Dyn.*, 2019, **6**, 064902.
170. K. S. Kjær, T. B. Van Driel, T. C. B. Harlang, K. Kunnus, E. Biasin, K. Ledbetter, R. W. Hartsock, M. E. Reinhard, S. Koroidov, L. Li, M. G. Laursen, F. B. Hansen, P. Vester, M. Christensen, K. Haldrup, M. M. Nielsen, A. O. Dohn, M. I. Pápai, K. B. Møller, P. Chabera, Y. Liu, H. Tatsuno, C. Timm, M. Jarenmark, J. Uhlig, V. Sundstöm, K. Wärnmark, P. Persson, Z. Németh, D. S. Szemes, É. Bajnóczi, G. Vankó, R. Alonso-Mori, J. M. Glowina, S. Nelson, M. Sikorski, D. Sokaras, S. E. Canton, H. T. Lemke and K. J. Gaffney, *Chem. Sci.*, 2019, **10**, 5749-5760.
171. M. Chergui and E. Collet, *Chemical Reviews*, 2017, **117**, 11025-11065.
172. J. Kern, R. Chatterjee, I. D. Young, F. D. Fuller, L. Lassalle, M. Ibrahim, S. Gul, T. Fransson, A. S. Brewster, R. Alonso-Mori, R. Hussein, M. Zhang, L. Douthit, C. de Lichtenberg, M. H. Cheah, D. Shevela, J. Wersig, I. Seuffert, D. Sokaras, E. Pastor, C. Weninger, T. Kroll, R. G. Sierra, P. Aller, A. Butryn, A. M. Orville, M. Liang, A. Batyuk, J. E. Koglin, S. Carbajo, S. Boutet, N. W. Moriarty, J. M. Holton, H. Dobbek, P. D. Adams, U. Bergmann, N. K. Sauter, A. Zouni, J. Messinger, J. Yano and V. K. Yachandra, *Nature*, 2018, **563**, 421-425.
173. V. Krewald, M. Retegan, N. Cox, J. Messinger, W. Lubitz, S. DeBeer, F. Neese and D. A. Pantazis, *Chem. Sci.*, 2015, **6**, 1676-1695.
174. M. Askerka, G. W. Brudvig and V. S. Batista, *Accounts of Chemical Research*, 2017, **50**, 41-48.
175. M. Suga, F. Akita, K. Yamashita, Y. Nakajima, G. Ueno, H. J. Li, T. Yamane, K. Hirata, Y. Umena, S. Yonekura, L. J. Yu, H. Murakami, T. Nomura, T. Kimura, M. Kubo, S. Baba, T. Kumasaka, K. Tono, M. Yabashi, H. Isobe, K. Yamaguchi, M. Yamamoto, H. Ago and J. R. Shen, *Science*, 2019, **366**, 334-338.
176. M. H. Cheah, M. Zhang, D. Shevela, F. Mamedov, A. Zouni and J. Messinger, *Proceedings of the National Academy of Sciences of the United States of America*, 2020, **117**, 141-145.
177. L. Young, K. Ueda, M. Gühr, P. H. Bucksbaum, M. Simon, S. Mukamel, N. Rohringer, K. C. Prince, C. Masciovecchio, M. Meyer, A. Rudenko, D. Rolles, C. Bostedt, M. Fuchs, D. A. Reis, R. Santra, H.

- Kapteyn, M. Murnane, H. Ibrahim, F. Légaré, M. Vrakking, M. Isinger, D. Kroon, M. Gisselbrecht, A. L'Huillier, H. J. Wörner and S. R. Leone, *Journal of Physics B: Atomic, Molecular and Optical Physics*, 2018, **51**, 032003.
178. P. Wernet, *Philos. Trans. R. Soc. A*, 2019, **377**, 20170464.
179. P. M. Kraus, M. Zürich, S. K. Cushing, D. M. Neumark and S. R. Leone, *Nature Reviews Chemistry*, 2018, **2**, 82-94.
180. M. Maiuri, M. Garavelli and G. Cerullo, *J. Amer. Chem. Soc.*, 2020, **142**, 3-15.
181. M. Mitrano, S. Lee, A. A. Husain, L. Delacretaz, M. Zhu, G. de la Peña Muñoz, S. X.-L. Sun, Y. I. Joe, A. H. Reid, S. F. Wandel, G. Coslovich, W. Schlotter, T. van Driel, J. Schneeloch, G. D. Gu, S. Hartnoll, N. Goldenfeld and P. Abbamonte, *Sci. Adv.*, 2019, **5**, eaax3346.
182. R. Geneaux, H. J. B. Marroux, A. Guggenmos, D. M. Neumark and S. R. Leone, *Philos. Trans. R. Soc. A-Math. Phys. Eng. Sci.*, 2019, **377**, 27.
183. D. Khakhulin, L. M. L. Daku, D. Leshchev, G. E. Newby, M. Jarenmark, C. Bressler, M. Wulff and S. E. Canton, *Physical Chemistry Chemical Physics*, 2019, **21**, 9277-9284.
184. Early Science at the Upgraded Advanced Photon Source,
<https://www1.aps.anl.gov/files/download/Aps-Upgrade/Beamlines/APS-U%20Early-Science-103015-FINAL.pdf>).



160x80mm (300 x 300 DPI)